3-D OPTICAL PROFILOMETRY AT MICRON SCALE WITH MODIFIED FIBER OPTIC LLOYD'S MIRROR TECHNIQUE

by
Arda İnanç
B.S., Physics, Boğaziçi University, 2017

Submitted to the Institute for Graduate Studies in
Science and Engineering in partial fulfillment of
the requirements for the degree of
Master of Science

Graduate Program in Physics
Boğaziçi University
2017

3-D OPTICAL PROFILOMETRY AT MICRON SCALE WITH MODIFIED FIBER OPTIC LLOYD'S MIRROR TECHNIQUE

APPROVED BY:

Prof. Mehmet Naci İnci (Thesis Supervisor)	.....
Prof. Mehmet Burçin Ünlü	.....
Assoc. Prof. Nüzhet Cenk Sesal	.....

DATE OF APPROVAL: 18.07.2017

ACKNOWLEDGEMENTS

Firstly, I would like to thank my advisor Prof. M. Naci İnci for his guidance and contributions to this project. Without him providing the opportunities, I would not be able to achive this work. I also express my gratitudes to my lab partners that are very kind and patient to me during this project.

In addition to all the instructors who have contributed to my experience and knowledge in many areas, I specially thank Prof. V. Erkcan Özcan for his wisdom in experimental physics and the guidance he has provided especially in this context whenever I needed. He is the one who convinced me to be an experimental physicist.

I would also like to thank my family and friends who have supported and endured many difficulties with me throughout my education life.

ABSTRACT

3-D OPTICAL PROFILOMETRY AT MICRON SCALE WITH MODIFIED FIBER OPTIC LLOYD'S MIRROR TECHNIQUE

In this thesis, it is shown that a modified fiber optic Lloyd's mirror technique is suitable and practical to produce fringe patterns that have easily adjustable frequency. This allows measuring 3D height distribution of test objects at micron scale without using additional elements as part of the optical projection unit.

To test the validity of the proposed method, images that contain deformed fringe patterns due to the height distribution of micron scale test objects are recorded by a CCD camera and analysed with one dimensional continuous wavelet transform. After the extraction of phase map using 1D continuous wavelet transform, the height distribution of the test objects is obtained by further analyses. Finally, the results are discussed and compared with the expected values.

ÖZET

MODİFİYE EDİLMİŞ FİBER OPTİK LLOYD AYNASI TEKNİĞİ İLE MİKRON ÖLÇEKTE ÜÇ BOYUTLU OPTİK PROFİLOMETRİ

Bu tezde, modifiye edilmiş fiber optik Lloyd ayna tekniğinin frekansı kolayca ayarlanabilir saçak desenleri üretmede uygun ve pratik olduğu gösterilmiştir. Bu, test objelerinin, optik projeksiyon ünitesi kapsamında ek elemanlar kullanılmaksızın mikron ölçekte üç boyutlu yükseklik dağılımını ölçme imkanı sağlamıştır.

Ortaya atılan metodun geçerliliğini kanıtlamak için mikron ölçekteki test objelerinin yükseklik dağılımından dolayı deforme olan saçak desenleri içeren resimler bir CCD kamera ile kayıt edilmiştir ve bir boyutlu, sürekli dalgacık dönüşümü ile analiz edilmiştir. Bir boyutlu sürekli dalgacık denklemi ile faz haritası çıkarımından sonra ileri analizler ile test objelerinin yükseklik dağılımı elde edilmiştir. Son olarak, sonuçlar tartışılmış ve beklenen değerlerle kıyaslanmıştır.

TABLE OF CONTENTS

LIST OF FIGURES

LIST OF SYMBOLS

a	Scaling parameter of mother wavelet
b	Translation parameter of mother wavelet
$\mathcal{F}$	Taking the fourier transform
$\hat{I}$	Fourier transform of I
Im	Taking the imaginary part
$\mathcal{M}_w$	Modulus array of $\mathcal{W}$
$\mathcal{P}_w$	Phase array of $\mathcal{W}$
Re	Taking the real part
$\mathcal{W}$	Wavelet transform of a signal
$\phi(x, y)$	Height related phase distribution
$\hat{\psi}$	Fourier transform of ψ

LIST OF ACRONYMS/ABBREVIATIONS

1D	One Dimensional
2D	Two Dimensional
3D & 3-D	Three Dimensional
CCD	Charge Coupled Device
CWT	Continuous Wavelet Transform
FFT	Fast Fourier Transform
FT	Fourier Transform
PSP	Phase Shifting Profilometry
WT	Wavelet Transform

1. INTRODUCTION

Since the optical profilers are fast, reliable and non-contact measurement systems, they have been used in many areas like medicine [1–3], automobile industry [4–6] and even in underwater applications [7]. Surface profile measurements using fringe projection techniques have gained more extensive interest over the years starting from 1983 in which Takeda proposed an automatic 3D shape measurement system [8]. It uses the *Fourier transformation* (FT) and triangulation method to extract the height distribution of objects. At that time, it was superior to Moiré pattern projection methods, which was firstly used in 1967 by Rowe and Welford [9]. Then, the researches have developed many methods like *Wavelet Transform* (WT) profilometry and *Phase Shifting Profilometry* (PSP), which are very common nowadays.

The optical profilometry applications are also used in a large range of scales from centimeter to subnanometer [10]. It is becoming important to use simple, cheap and fast methods to achive reasonable precision in desired scales.

In this thesis, we developed a cheap and simple to construct system for 3D profilometry at micron scale. By doing a small modification to *Lloyd's mirror* technique, it becomes easy to study the height distributions of test objects at micron scale.

In the following chapters, firstly, a review for fringe pattern generation techniques and the analysis types used for generated fringe patterns is given to a finite extent. Then, the newly introduced technique for fringe pattern generation is depicted and the theory behind it is shown in detail. After, the analyses used for the newly generated fringe patterns are given step by step while it is supported with the experimental data. Lastly, the height measurement results of various test objects and discussions are presented.

2. REVIEW

Optical profilometry is a powerful, non-contact and fast technique to extract the three dimensional shapes of object surfaces. There are two main categorization of the optical profilometry types, namely intensity and phase types. Confocal technology [11] and Phase-shifting interferometry [12] are the well known examples of them. In optical profilometry, height information of the surfaces can be acquired by scanning the object point by point [13], layer by layer [14] or just with a single two dimensional image, which is called full field of view [15]. Since the field is very diverse and it is related to our work, the phase-type optical profilometry techniques are the main focus of this review work.

There is a more detailed categorization in [16] but one can categorize the phase-type optical profilometry techniques, that takes the two dimensional image of the object surface, according to the methods used to generate the deformed fringe patterns that carry information about the height distribution of a test surface and to analysis types of phase retrieval from data.

2.1. Generation Types of Deformed Fringe Patterns

In this section, the most common fringe pattern generation types are presented. Generation of fringe patterns can be divided into two categories: interferometric optical profilometry and fringe projection profilometry.

2.1.1. Interferometric Optical Profilometry

In interferometric optical profilometry techniques, a coherent light source and a mechanism to separate the light into two beams are used. One of them is the reference beam and the other one is the beam that is reflected from the test object. Then, both light beams are combined to generate sinusoidal fringe patterns where there are deformations due to the height distribution on the surface of the object.

A beam splitter is used to separate the incident light into two arms, namely reference and test arms. With a mirror at the end of the reference arm, light in the reference arm is reflected back to the beam splitter while the object surface reflects the incoming light back to the same beam splitter; thus, the interference pattern is generated with the interference of the light waves coming from both arms. The combined fringe pattern is observed with a camera placed at the back of the beam splitter. This type of interferometer is called the *Michelson interferometer* and a sketch is illustrated in Figure 2.1 [17].

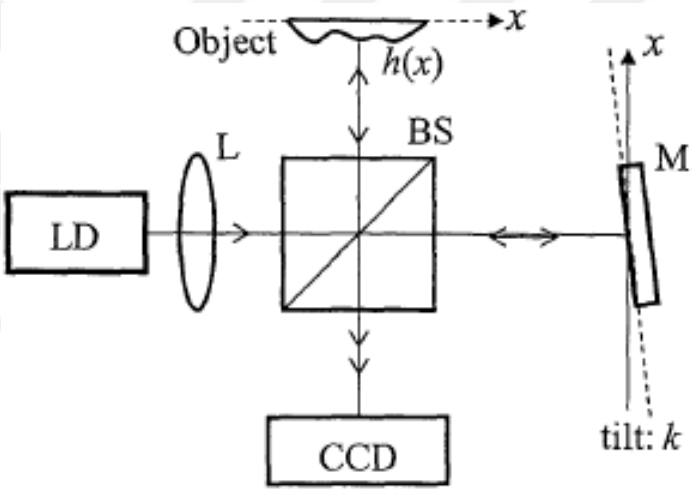

Figure 2.1. Michelson interferometer [17].

For small surfaces where high magnification lenses are needed, *Linnik interferometer* is used. The system can be seen in Figure 2.2 [9]. It consists a beam splitter which divides the light into two and sends onto two different objective lenses. One of the objective lenses is for the reference beam where there is a mirror at the end of the objective lense, the other objective lens is to focus the test beam on to the test object and to get the reflected light back to combine it with the reference beam reflected from the mirror to make an interference pattern. Using second objective in the reference arm is beneficial to eliminate the optical aberrations stemming from the objective lens focusing on the test surface.

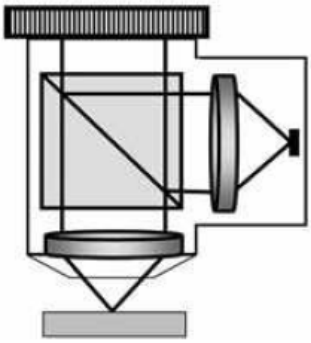

Figure 2.2. Linnik interferometer [9].

An interesting setup including a small endoscope is constructed by using *Spectral interferometry* [18]. Laser pulses are divided into reference and test arms with a grating-lens system. Signal is encoded with the height distribution of the test surface and merged with the signal from the reference arm. Then, it is decoded again with a grating-lens system to retrieve a fringe pattern on a CCD camera. A schematic of the device is shown in Figure 2.3.

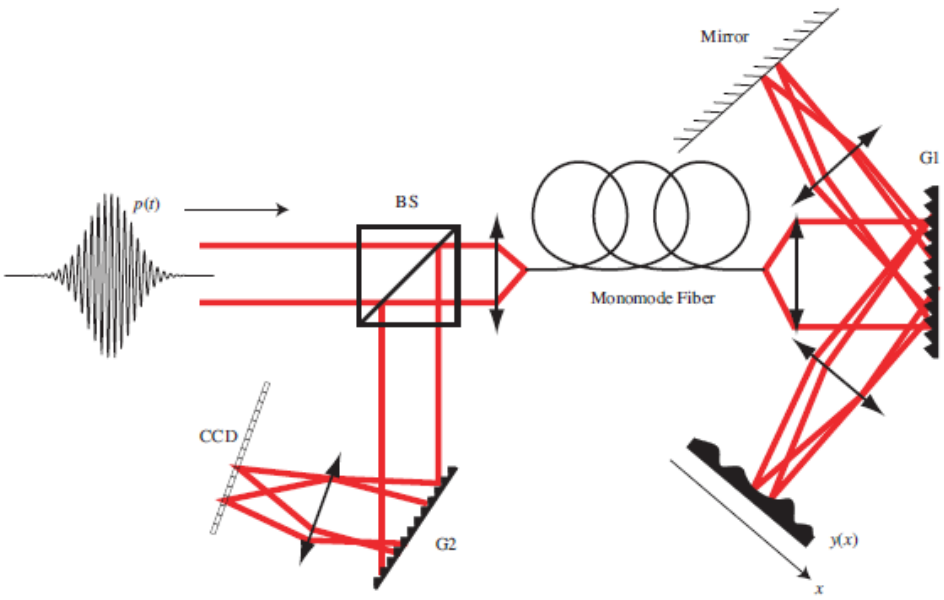

Figure 2.3. An application of spectral interferometer [18].

As it is seen in the above interferometer types, deformed fringe patterns are constructed on the camera or at the point of observation via merging the two beams with different information (reference and object related). In the next subsection, the methods that fringe patterns are formed and projected directly on to the object surface are mentioned.

2.1.2. Fringe Projection Profilometry

In this profilometry method, interferometric approaches like the above examples are used to generate the fringe patterns but the resultant fringe patterns do not carry information about the height distribution of the test surface like as in the previous deformations. In this technique, fringe patterns generated and projected on to the object surface and the resultant deformations due to the height distribution of the test subject are observed directly by inspecting the surface of the object since the fringes are physically deformed on the surface of the test object. Both coherent and white light sources can be used in this profilometry type.

Mirau interferometer is a system like Michelson interferometer but the test and reference arms are in a compact form inside a microscope objective as seen in Figure 2.4 [9]. This is needed for smaller test objects since the working distance of the objective lenses used is getting smaller where it is hard to put a traditional beam splitter and a reference mirror between the objective lens and the test surface.

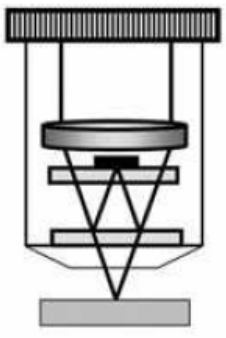

Figure 2.4. Mirau interferometer [9].

There is a fringe projection profilometry type that is compact like Mirau interferometer which is called *Fabry-Pérot interferometer*. Two partially reflective surfaces inside a cavity as in Figure 2.5 [19] that are positioned nearly parallel used in this method to generate undeformed fringe patterns. Light waves that are reflected back and forth from the reflective surfaces interfere with the newly incoming light waves and leave the cavity. According to the characteristics of the cavity, undeformed fringe patterns are formed at the end of the Fabry-Pérot system and are projected on to the test surface. Then, deformed fringe patterns on the object surface are recorded with an image acquisition device [20].

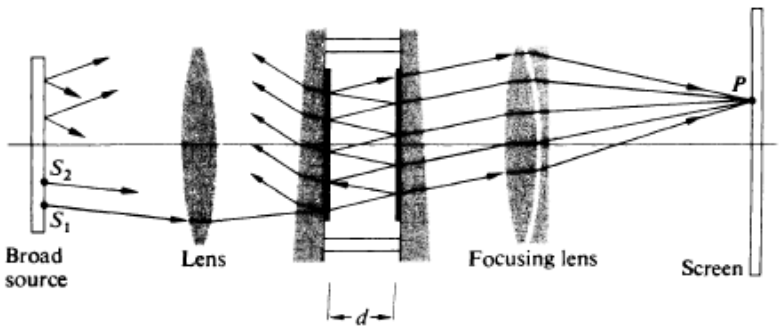

Figure 2.5. Fabry-Pérot interferometer [19].

Apart from the interferometric techniques, there is a more compact and simple system that uses the cores of a four-core optical fiber to propagate light waves and make them interfere with each other to generate a fringe pattern at the exit of the optical fiber [21]. It does not require any beam splitters or mirror like reflective surfaces. As an optical element, only a lens is used to collimate the cone shaped light coming from the fiber as shown in Figure 2.6. Resulted pattern is different than the two beam interference patterns (periodic dots in both directions instead of lines since this is a kind of a four beam interference pattern), but it can be projected on a test subject and recorded with a CCD camera to study the deformations on the fringe pattern. By calibration or revealing the optical dynamics of the system and analyzing the phase of the deformed pattern, one can get the height distribution of the test object.

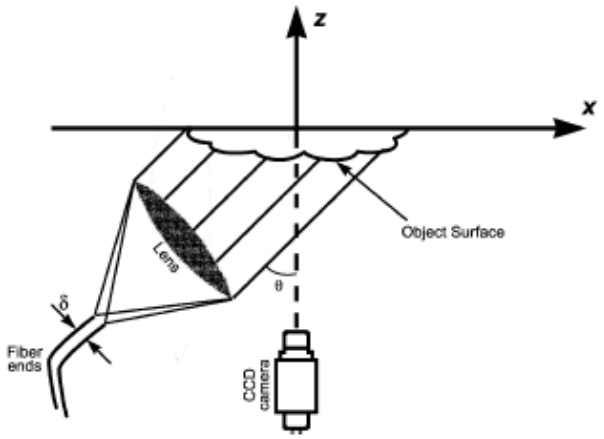

Figure 2.6. Fringe pattern generation with four-core optical fiber [21].

A similar fringe pattern generation system like double-slit can be constructed by dividing the light waves that are guided in a single-core fiber, into two arms by using a fiber optic coupler at the end of the single-core fiber and make them interfere at the exit of the coupler as depicted in Figure 2.7 [22].

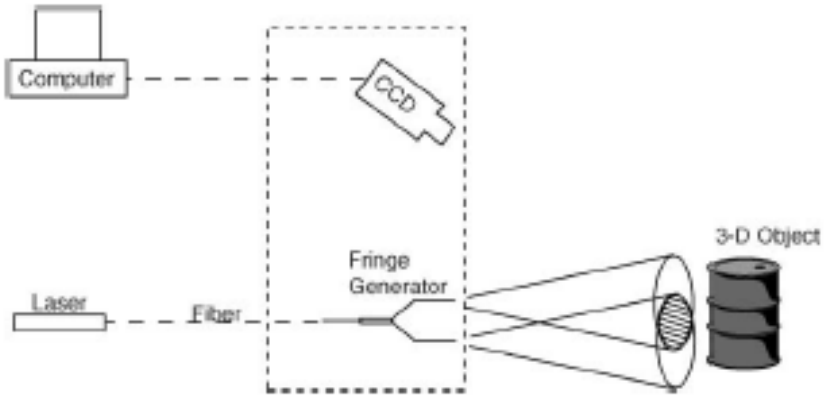

Figure 2.7. Fringe pattern generation using a fiber optic coupler [22].

With the help of gratings, which are composed of many slits, one can also generate fringe patterns. Using a grating or two in a stereo microscope as in Figure 2.8 can be an example of fringe projection profilometry at micron scale [23]. These are specially designed binary gratings to get an ideal sinusoidal intensity on fringe patterns.

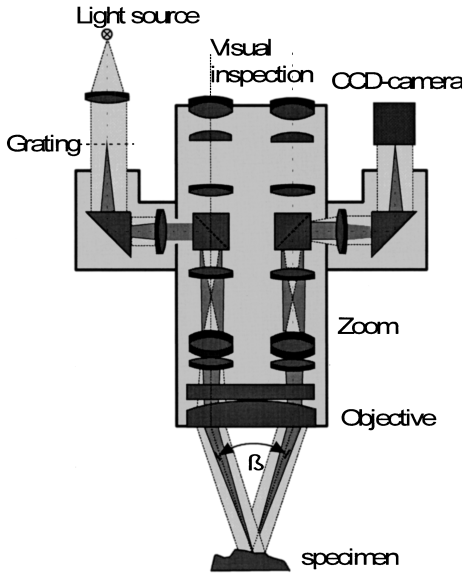

Figure 2.8. An example of stereo microscope with fringe projection unit [23].

Another fringe projection method is using *Moiré pattern*. It can be generated using two gratings as in Figure 2.9 [9]. By moving the gratings slightly relative to each other, one can obtain fringes with different frequencies and shift the phase of the fringes. It is a method used in phase-shifting profilometry [24].

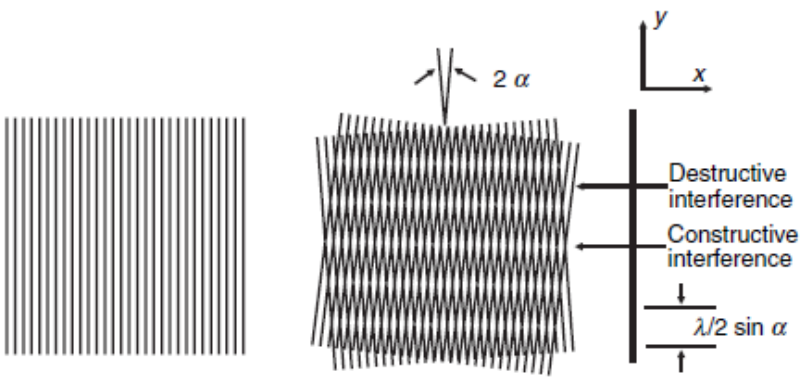

Figure 2.9. Generation of Moiré pattern with gratings [9].

Recently, another common fringe projection method is used to study the height distribution of the objects. The method generates fringe patterns digitally where there

are no physical methods as before. That is called digital fringe projection profilometry [25–27]. This method of fringe pattern generation has many different kinds since one can project any analyzable structured light pattern which is simulated by a computer software. Some of them project generated sinusoidal patterns or Moiré patterns which can be acquired by superimposing two linear fringe patterns with different periods as in Figure 2.10 [28]. In some cases, binary coded patterns are used instead of sinusoidal patterns and needs other analysis methods [29] but sometimes they are turned into sinusoidal patterns by defocusing [30] or by superpositioning different number of binary coded patterns [31] to analyse them with the traditional methods used for sinusoidal fringe patterns.

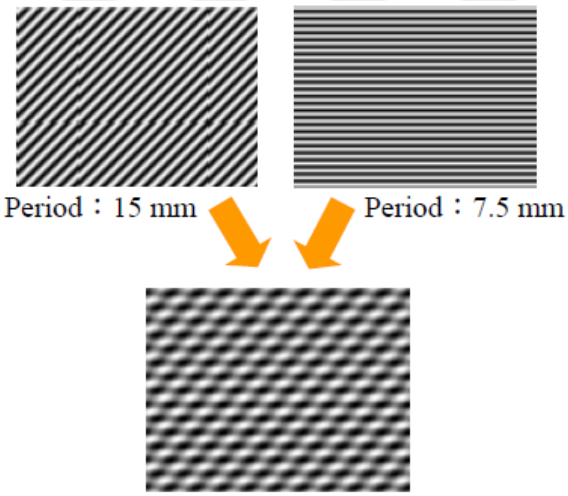

Figure 2.10. Computer simulated Moiré pattern [28].

There are also marker encoded [32] and color coded binary [33] fringe patterns to get detailed information about the height distribution by identifying the fringe order and to reduce the phase related errors. This can clarify the 2π ambiguities, which stem from the large height variations (discontinuities) that shift the fringes π or more. One can check the review paper [34] about the structured light patterns to learn the drawbacks and advantages of using them or more.

Lastly, there is the fringe projection method we applied in our experiments which uses *Lloyd's mirror* technique. In this setup, there is a monochromatic, point light

source and an image of it produced by a mirror so both light waves can generate an interference pattern like in the double slit experiment. As in Figure 2.11, a fiber optic cable is used to guide the light from a coherent light source like a laser to the mirror used so the projected pattern can be directed easily [35].

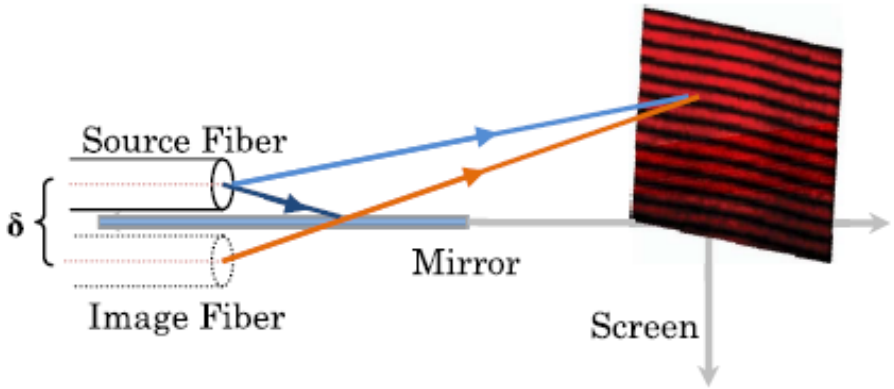

Figure 2.11. Example sketch of Lloyd's mirror technique [35].

2.2. Phase Analysis Types of Deformed Fringe Patterns

In this section, fundamental, 1D theories used to analyze phase distribution of deformed sinusoidal fringe patterns, generated by one of the methods above, are discussed.

For a general case, two separated waves from a coherent light source have the intensity function as in Equation 2.1, which is given as [36].

$$I' = 2I'_0 \left(1 + \cos(\Delta\Theta)\right) \tag{2.1}$$

I'_0 is the intensity of both waves and $\Delta\Theta$ is the phase difference between them.

$$I(x, y) = I_0(x, y) \left[1 + V(x, y) \cos(2\pi f_0 x + \phi(x, y))\right] \tag{2.2}$$

The fringe signal which is recorded and processed, can be expressed in the form of Equation 2.2 [37]. In this equation, $I_0(x, y)$ represents background noise, $V(x, y)$ is the fringe visibility, f_0 is the spatial carrier frequency in the x-direction and $\phi(x, y)$ is the height related phase distribution causing the deformation on the fringe pattern. $I_0(x, y)$, $V(x, y)$ and $\phi(x, y)$ are assumed to be very slowly varying functions in x compared to the variations introduced by $2\pi f_0 x$ term. To extract the phase of the signal, all the analysis techniques below use this intensity function or its modifications resulting from the fringe projection and acquisition techniques.

2.2.1. Fourier Transform Analysis

In Fourier analysis, we simply take the Fourier transform of the intensity function. By using Euler's formula, one can obtain an exponential representation of the function $\cos(2\pi f_0 x + \phi(x, y))$ as follows:

$$e^{i\theta} = \cos(\theta) + i\sin(\theta)$$

$$\cos(\theta) = \frac{e^{(i\theta)} + e^{-(i\theta)}}{2} \tag{2.3}$$

$$\cos(2\pi f_0 x + \phi(x, y)) = \frac{e^{i(2\pi f_0 x + \phi(x,y))} + e^{-i(2\pi f_0 x + \phi(x,y))}}{2}$$

With the definitions of new terms like $a(x, y) \equiv I_0(x, y)$ and $b(x, y) \equiv I_0(x, y)V(x, y)$ and by using the expanded form of the last equation derived above, Equation 2.2 is expressed as

$$I(x, y) = a(x, y) + \frac{b(x, y)}{2}\left(e^{i(2\pi f_0 x)}e^{i\phi(x,y)} + e^{-i(2\pi f_0 x)}e^{-i\phi(x,y)}\right) \tag{2.4}$$

Now 1D Fourier transform of the intensity function in Equation 2.4 is taken with respect to x; where $\hat{I}(f, y)$ is the fourier transform of $I(x, y)$.

$$\mathcal{F}(I(x,y)) = \hat{I}(f,y) = \int_{-\infty}^{\infty} I(x,y)e^{-i(2\pi fx)}\,dx$$

$$= \int_{-\infty}^{\infty} a(x,y)e^{-i(2\pi fx)}\,dx + \int_{-\infty}^{\infty} \frac{b(x,y)}{2}e^{i(2\pi f_0 x)}e^{i\phi(x,y)}e^{-i(2\pi fx)}\,dx \tag{2.5}$$

$$+ \int_{-\infty}^{\infty} \frac{b(x,y)}{2}e^{-i(2\pi f_0 x)}e^{-i\phi(x,y)}e^{-i(2\pi fx)}\,dx$$

where f is the spatial frequency in the x direction. $a(x,y)$, $b(x,y)$ and exponential functions with $\phi(x,y)$ are taken outside the integrals as they are assumed to be constants with respect to x. It is due to approximating them to the first terms of the three functions in Taylor Expansion since they are very slowly varying functions compared to f_0 and f. Therefore, Equation 2.5 becomes

$$\hat{I}(f,y) \approx a(y)\int_{-\infty}^{\infty} e^{-i(2\pi fx)}\,dx + \frac{b(y)}{2}e^{i\phi(y)}\int_{-\infty}^{\infty} e^{i(2\pi f_0 x)}e^{-i(2\pi fx)}\,dx$$

$$+ \frac{b(y)}{2}e^{-i\phi(y)}\int_{-\infty}^{\infty} e^{-i(2\pi f_0 x)}e^{-i(2\pi fx)}\,dx \tag{2.6}$$

$$\delta(f) = \int_{-\infty}^{\infty} e^{-i(2\pi fx)}\,dx \tag{2.7}$$

By collecting the similar terms and reminding the definition of $\delta(f)$ function in frequency domain as in Equation 2.7, Equation 2.8 is obtained as

$$\hat{I}(f,y) \approx a(y)\delta(f) + \frac{b(y)}{2}e^{i\phi(y)}\delta(f-f_0) + \frac{b(y)}{2}e^{-i\phi(y)}\delta(f+f_0) \tag{2.8}$$

All the terms on the right-hand side of Equation 2.8 are defined as

$$A(f,y) \equiv a(y)\delta(f), \qquad C(f,y) \equiv \frac{b(y)}{2} e^{i\phi(y)} \delta(f) \tag{2.9}$$

also by using the proper variable change from f to $f - f_0$ and using the complex conjugate Equation 2.10 is arrived as

$$\hat{I}(f,y) = A(f,y) + C^*(f + f_0, y) + C(f - f_0, y) \tag{2.10}$$

All the three terms here are the modulations of the δ function where the first term is at the origin while the others are at a distance f_0 apart from the origin on both sides. First term and one of the other terms are not necessary to get the height distribution related component of the phase. The right term in Equation 2.10 is carved out with a band-pass filter and is shifted to the origin,as the middle and the left terms are filtered out, as sketched in Figure 2.12 [8].

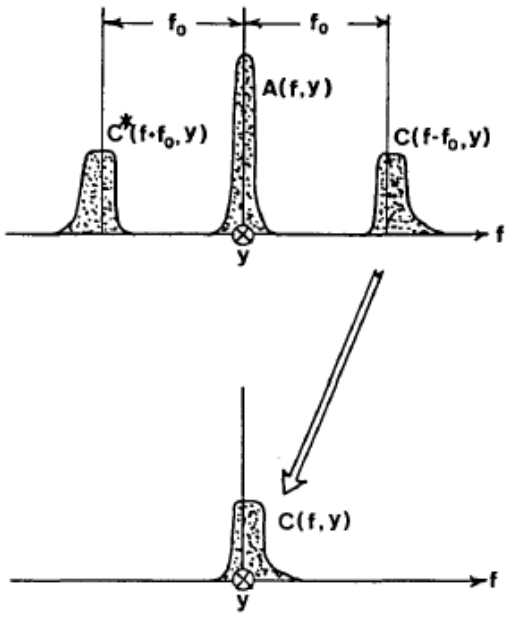

Figure 2.12. Translation of a single spectrum of the fourier analysed signal [8].

$C(f, y)$ is transformed back with the inverse Fourier transform, which gives us

$$\mathcal{F}^{-1}(C(f, y)) = c(x, y) = \frac{b(x, y)}{2} e^{i\phi(x,y)} \tag{2.11}$$

Spatial carrier frequency f_0 and the background intensity are eliminated here. To get the phase $\phi(x, y)$, one can either separate the imaginary and the real part by taking the natural logarithm of both sides of Equation 2.11 as

$$\log c(x, y) = \log\left(\frac{b(x, y)}{2}\right) + i\phi(x, y) \tag{2.12}$$

One may select the imaginary part, or after expanding the exponential in $c(x, y)$ with the Euler's formula, and directly take the imaginary part and divide it by the real part of $c(x, y)$ and then take the arctangent as shown in Equation 2.13:

$$\arctan\left(\frac{Im(c(x, y))}{Re(c(x, y))}\right) = \arctan\left(\frac{\frac{b(x,y)}{2}\sin(\phi(x, y))}{\frac{b(x,y)}{2}\cos(\phi(x, y))}\right) = \phi(x, y) \tag{2.13}$$

However, due to the nature of the arctangent, the phase will be wrapped in x between π and $-\pi$. Therefore, an unwrapping algorithm is needed to recover the phase. 1D and 2D wrapped and unwrapped phase examples are illustrated in Figure 2.13 and Figure 2.14 [38]. After extracting the phase of the object, the data is converted into height distribution with proper calibration methods as introduced in [39].

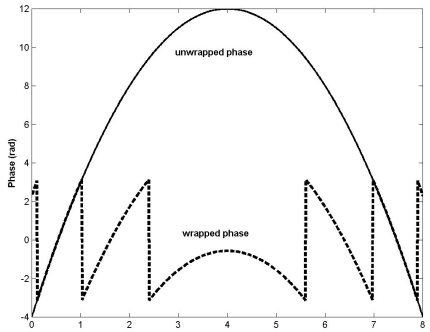

Figure 2.13. 1D wrapped and unwrapped phase example [38].

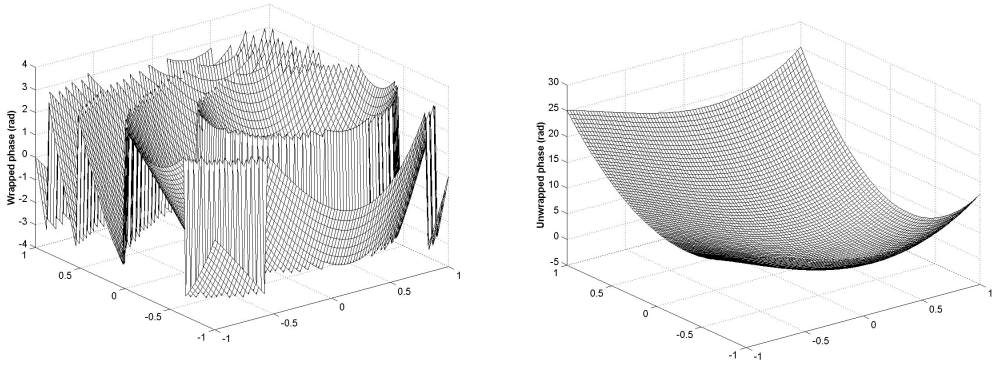

Figure 2.14. 2D wrapped and unwrapped phase example [38].

There exist different improved types of Fourier analysis methods such as the extension of Fourier transform like windowed [40], interpolated [41] and regressive Fourier transform [42]. They can produce more accurate phase results than FT alone, but face different problems. For example, windowed Fourier transfrom can analyze the fringe pattern locally unlike the FT method, but it cannot give accurate results for rapidly changing spatial frequencies (limited resolution in frequency domain) because of the fixed size of the window used [43].

The next analysis type, which is using wavelet transform, overcomes not only the problems mentioned above and more but also can benefit from the power of the fast Fourier transform (FFT) algorithm. An additional function called mother wavelet is used in the transformation to extract the intensity function local by local. Any leakage in an area on the image that is caused by discontinuities or high surface slope of the test object can propagate as an error on the whole image in FT method due to the global processing nature of it, whereas mother wavelet in WT prevents this propagation of error and makes the leakage stay in that area. In FT, also the number of fringes on the analyzed image should be integer to prevent leakage from the borders and the deformed intensity signal should be periodic [44]. These problems are not restrictions in WT. However, one should choose the mother wavelet wisely since their powers differ according to the characteristics of the analyzed image, test object and the fringe pattern.

2.2.2. Wavelet Transform Analysis

Wavelet transform can be divided into two categories namely *discrete wavelet transform* and *continuous wavelet transform* (CWT). For continuous wavelet transformation, nonorthogonal wavelet functions are used, whereas orthogonal sets of functions are used for discrete wavelet transform [45]. Since our intensity function is a continuous 2D signal, continuous wavelet transform in one dimension is reviewed in this part. The phase of a row (constant y) of the 2D signal is evaluated. After the phase is extracted for a row of the signal, it can be repeated row by row on the whole image to get the 2D phase of the signal.

For 1D intensity signal of a row, we have the following equation by eliminating the y components of the terms in Equation 2.2:

$$I(x) = I_0(x)\left[1 + V(x)\cos(2\pi f_0 x + \phi(x))\right] \tag{2.14}$$

To recover the phase, the carrier frequency f_0 should satisfy the following condition [46].

$$2\pi f_0 > \left|\frac{d\phi(x)}{dx}\right|_{max} \tag{2.15}$$

1D CWT of a continuous, 1D intensity signal $I(x)$ is defined as

$$\mathcal{W}(a,b) = \frac{1}{\sqrt{a}}\int_{-\infty}^{\infty} I(x)\psi^*\left(\frac{x-b}{a}\right)dx \tag{2.16}$$

It is the convolution of the signal with $\psi^*\left(\frac{x-b}{a}\right)$ which is the complex conjugate, scaled and translated version of a mother wavelet $\psi(x)$. Here a (> 0) and b are real, scaling and translation parameters of the wavelet respectively.

To be treated as a wavelet, the following three criteria [47] must be satisfied.

(i) To have a local nature, a mother wavelet must be centered at zero and satisfy :

$$\int_{-\infty}^{\infty} |\psi(x)|^2 \, dx < \infty$$
$$\lim_{|x|\to\infty} \psi(x) = 0 \tag{2.17}$$

(ii) It must be invertible. If $\hat{\psi}(f)$ is the Fourier transform of $\psi(x)$ like:

$$\hat{\psi}(f) = \int_{-\infty}^{\infty} \psi(x) e^{-i(2\pi f x)} \, dx \tag{2.18}$$

the following equation must hold:

$$\int_{0}^{\infty} \frac{|\hat{\psi}(f)|^2}{f} \, df < \infty \tag{2.19}$$

Equation 2.19 is called admissibility condition and implies that the mother wavelet has no frequency component that is zero ($\hat{\psi}(0) = 0$), so the original signal can be obtained with an inverse transformation.

(iii) For complex wavelets, the Fourier transform of the wavelet, $\hat{\psi}(f)$, must be real and vanish for negative frequencies:

$$\hat{\psi}(f < 0) = 0 \tag{2.20}$$

By eliminating the confusion about negative frequencies, we simplify the interpretation of the transform [48].

After the determination of the mother wavelet $\psi(x)$ that satisfies the above criteria, one can solve the integral for the phase term or to be able to use the fast Fourier transform algorithm, and rewrite the Equation 2.16 in Fourier space by using the *Parseval's theorem* [49] as follows:

Using the definitions of the inverse Fourier transform of both functions:

$$I(x) = \int_{-\infty}^{\infty} \hat{I}(h) e^{i2\pi hx}\, dh, \qquad \psi(x) = \int_{-\infty}^{\infty} \hat{\psi}(f) e^{i2\pi fx}\, df \tag{2.21}$$

and with the variable change of $x \to \frac{x-b}{a}$ and $\frac{f}{a} \to g$ $\left(\frac{df}{a} = dg\right)$, one obtains

$$\begin{aligned} \psi\left(\frac{x-b}{a}\right) &= \int_{-\infty}^{\infty} \hat{\psi}(f) e^{i2\pi f\left(\frac{x-b}{a}\right)}\, df \\ &= \int_{-\infty}^{\infty} \hat{\psi}(f) e^{i2\pi f\frac{x}{a}} e^{-i2\pi f\frac{b}{a}}\, df \\ &= \int_{-\infty}^{\infty} \hat{\psi}(ag) e^{i2\pi gx} e^{-i2\pi gb} a\, dg \end{aligned} \tag{2.22}$$

By substituting $I(x)$ and $\psi^*\left(\frac{x-b}{a}\right)$ in Equation 2.16 and rearranging the terms give us

$$\begin{aligned} \mathcal{W}(a,b) &= \frac{1}{\sqrt{a}} \int_{-\infty}^{\infty} dx \int_{-\infty}^{\infty} \hat{I}(h) e^{i2\pi hx}\, dh \int_{-\infty}^{\infty} \hat{\psi}^*(ag) e^{-i2\pi gx} e^{i2\pi gb} a\, dg \\ &= \frac{a}{\sqrt{a}} \int_{-\infty}^{\infty} \int_{-\infty}^{\infty} \int_{-\infty}^{\infty} \hat{I}(h) \hat{\psi}^*(ag) e^{i2\pi hx} e^{-i2\pi gx} e^{i2\pi gb}\, dh\, dg\, dx \\ &= \sqrt{a} \int_{-\infty}^{\infty} \int_{-\infty}^{\infty} \hat{I}(h) \hat{\psi}^*(ag) e^{i2\pi gb}\, dh\, dg \int_{-\infty}^{\infty} e^{i2\pi(h-g)x}\, dx \end{aligned} \tag{2.23}$$

The last integral is $\delta(g-h)$, which is also equal to $\delta(h-g)$, so we get

$$\mathcal{W}(a,b) = \sqrt{a}\int_{-\infty}^{\infty}\int_{-\infty}^{\infty}\hat{I}(h)\hat{\psi}^{*}(ag)e^{i2\pi gb}\,dh\,dg\delta(h-g)$$

$$= \sqrt{a}\int_{-\infty}^{\infty}\hat{\psi}^{*}(ag)e^{i2\pi gb}\,dg\int_{-\infty}^{\infty}\hat{I}(h)\delta(h-g)\,dh \tag{2.24}$$

$$= \sqrt{a}\int_{-\infty}^{\infty}\hat{\psi}^{*}(ag)e^{i2\pi gb}\,dg\hat{I}(g)$$

Equation 2.25, which is 1D CWT of the signal $I(x)$ in Fourier space and is equivalent to Equation 2.16:

$$\mathcal{W}(a,b) = \int_{-\infty}^{\infty}\hat{I}(g)\hat{\psi}^{*}_{a,b}(g)\,dg \tag{2.25}$$

where $\hat{\psi}^{*}_{a,b}(g) = \sqrt{a}\hat{\psi}^{*}(ag)e^{i2\pi gb}$

In this form, the 1D CWT of the signal using fast Fourier transform algorithm is discretely computed. For every row of the intensity signal, after taking its Fourier transform, algorithm gives us a 2D, complex array with the coordinates a and b. To extract the phase of the 2D signal, the modulus and the phase of this complex array $\mathcal{W}(a,b)$ for every row of the image is examined. They are calculated, respectively, as follows:

$$\mathcal{M}_{w}(a,b) = |\mathcal{W}(a,b)| = \sqrt{[Re(\mathcal{W}(a,b))]^2 + [Im(\mathcal{W}(a,b))]^2} \tag{2.26}$$

$$\mathcal{P}_{w}(a,b) = arg(\mathcal{W}(a,b)) = \arctan\left(\frac{Im(\mathcal{W}(a,b))}{Re(\mathcal{W}(a,b))}\right) \tag{2.27}$$

Modulus array in Equation 2.26 is the amplitude of the complex array $\mathcal{W}(a,b)$. It gives the similarity between the signal and the wavelet, since it is maximum when

the signal and the wavelet are matched [50]. Thus, one can check the positions of the maximum points on the modulus array for all the b values to make an estimation about the phase of the signal after looking those corresponding positions in the phase array. For a fixed b value on the horizontal axis in the modulus array, the element a_r with the maximum value is called ridge point. The path constructed by determining all the maximum points for every b value is called the ridge array. This gives a and b coordinates where the phase of the signal and the phase of the wavelet are very similar. An example of the ridge array extraction from the modulus array and choosing that coordinates on the phase array can be seen in Figure 2.15 [51]. White color in modulus array indicates higher values whereas the black represents lower values.

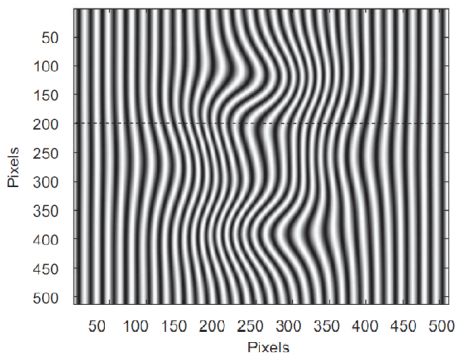

(a) Choosen row from the image.

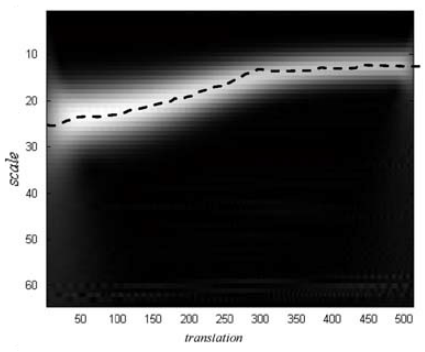

(b) Modulus array of the row chosen.

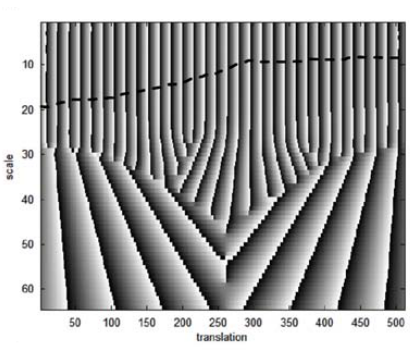

(c) Phase array of the row chosen.

Figure 2.15. An example of determination and selection of the ridge array from a row of an analysed image [51].

The phase of a row of the signal is:

$$\mathcal{P}_{wr}(a_r(b), b) = arg(\mathcal{W}_r(a_r(b), b)) = \arctan\left(\frac{Im(\mathcal{W}_r(a_r(b), b))}{Re(\mathcal{W}_r(a_r(b), b))}\right) \tag{2.28}$$

Then, it is repeated for every row of the image to get the phase of the whole, 2D image. However, due to the nature of the inverse tangent function in Equation 2.27, again there are jumps in the phase from $-\pi$ to π values and it should be unwrapped with an unwrapping algorithm. After the unwrapping, the phase of the whole signal which is equal to the term $2\pi f_0 x + \phi(x, y)$ inside the cos function in Equation 2.2 is obtained.

To get the height related phase distribution $\phi(x, y)$, we need to remove $2\pi f_0 x$ term, which is called carrier removal. In FT analysis, it is done when we select and translate a single spectrum as in Figure 2.12.

In WT, various methods can be used for carrier removal as stated in [52]. Linear carrier removal methods like plane fitting and average slope approach can be utilised since f_0 is a constant. However, sometimes f_0 is not a constant and may change along the projection axis, e.g., $f_0(x)$ with a nonlinear relation on the projection axis; or a nonlinear deformation on the phase can occur due to a problem on the image acquisition system like optical aberrations and distortions caused by an objective lens. In this case, one should use nonlinear carrier removal techniques like reference subtraction, phase mapping, second order surface fitting, series expansion methods or a new method as in [53] to achieve better results. After extracting the phase in radians, one of the calibration techniques is used to get the height distribution of the object.

An example of applying a linear and a nonlinear carrier removal technique to an unwrapped image is demonstrated in Figure 2.16, where the carrier is not linear [54]. All methods have different advantages and disadvantages. One must choose a method according to their needs.

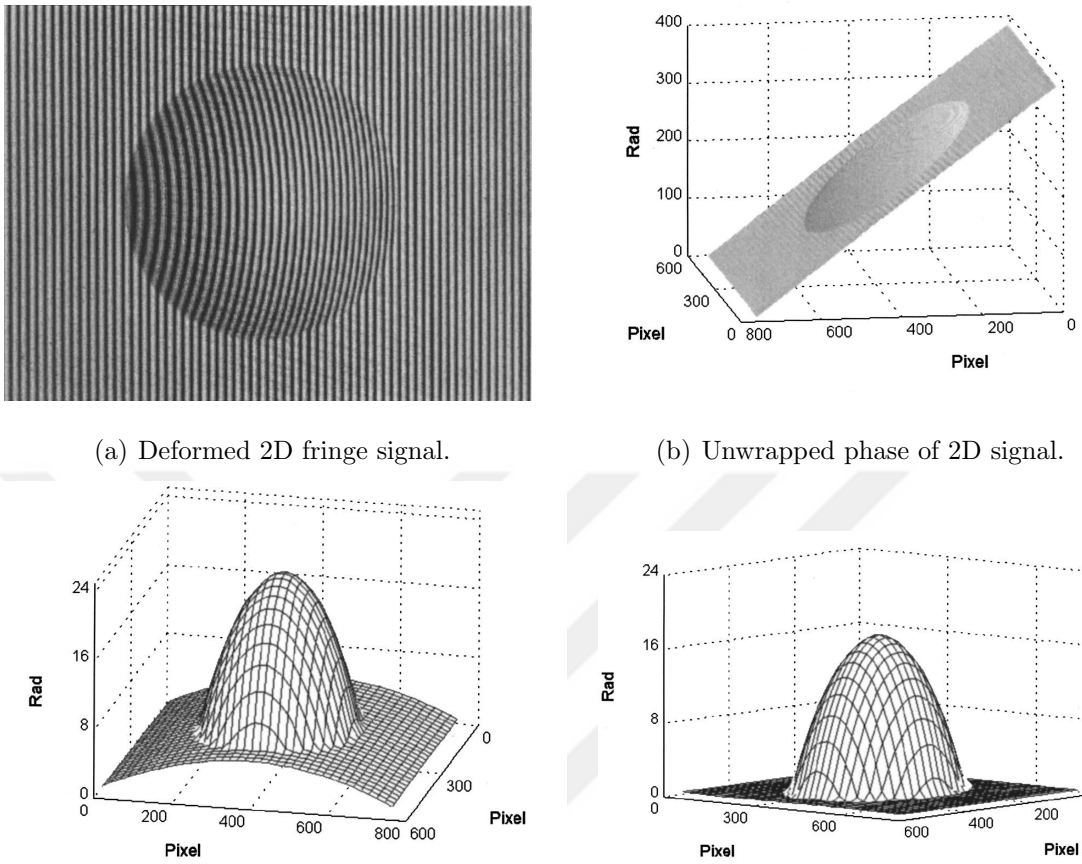

(a) Deformed 2D fringe signal.

(b) Unwrapped phase of 2D signal.

(c) Phase after linear carrier removal.

(d) Phase after nonlinear carrier removal.

Figure 2.16. An example on linear and nonlinear carrier removal [54].

As opposed to FT analysis, WT analysis is more noise insensitive since FT processes a signal globally whereas WT uses the local features of the wavelets. The chosen mother wavelet for WT analysis is also important in terms of noise, signal frequency and discontinuities on the fringe pattern due to sudden changes in the height of the test object. Apart from being discrete and continuous, there are both real and complex valued (analytical) mother wavelets. However, as stated in [55], using continuous complex mother wavelets gives better results than using real or discrete wavelet functions. Some of common and continuous complex mother wavelets used in fringe pattern analaysis are *Morlet wavelet* [17], *Paul wavelet* [56], *Mexican hat wavelet* [57] and newly introduced *Generalized Morse wavelet* [58]. Since it is very well localized in both time and space domains, Morlet wavelet and 1D CWT is employed in our analysis.

To mention briefly, there is also a common technique for phase extraction called *Phase Shifting Profilometry*(PSP). It uses three or more pictures which have equally phase shifted fringe patterns with a constant phase value like $\left(\frac{\pi}{2}\right)$ as in [59]. The phase analysis of PSP is quite simple and straight forward: For example, the term inside the cosine term of the intensity function can be calculated by using three phase shifted intensity functions extracted from three different images as in Equation 2.29. The retrieved phase again needs unwrapping and carrier removal.

$$2\pi f_0 x + \phi(x,y) = \arctan\left(\frac{I_2 - I_3}{I_2 - I_1}\right) \tag{2.29}$$

where intensity functions I_i have a difference of $\left(\frac{\pi}{2}\right)$ like:

$$\begin{aligned} I_1(x,y) &= I_0(x,y)\left[1 + V(x,y)\cos(2\pi f_0 x + \phi(x,y))\right] \\ I_2(x,y) &= I_0(x,y)[1 + V(x,y)\cos(2\pi f_0 x + \phi(x,y) + \frac{\pi}{2})] \\ I_3(x,y) &= I_0(x,y)\left[1 + V(x,y)\cos(2\pi f_0 x + \phi(x,y) + \pi)\right] \end{aligned} \tag{2.30}$$

The resolution of this technique increases as the number of images taken increases. However, one should bare in mind that it is difficult to calibrate and produce these exact phase shifts and it is time consuming to capture and process multiple images.

3. EXPERIMENTAL

In this chapter, first of all, details about our optical profilometry setup and the fringe pattern generation method are introduced. Secondly, used analyses to extract phase map and height distribution of objects from the deformed fringe patterns are discussed in depth.

3.1. Fringe Projection with Lloyd's Mirror Technique at Micron Scale

3.1.1. Setup

Instead of constructing sinusoidal patterns from digital patterns with different techniques mentioned in the review chapter, nature of interference is employed to obtain almost perfect and easily generated sinusoidal fringe signals with a fiber optic Lloyd's mirror method. Such technique is briefly mentioned in the review chapter and is the method used in our experimental work here in this theis. Light coming from a monochromatic coherent source, that is, a HeNe laser with 632.8 nm wavelength, is coupled into a single mode fiber optic cable by a 3D micro-stage launcher. Then, the other end of the fiber, which emits the guided waves as a cone of light is placed onto a flat ordinary mirror. Since the fiber end is very closely placed on the mirror, it acts like a point source. Such an assembly is basically called fiber optics Lloyd's mirror.

One would need a smaller fringe spacing to perform micron scale measurements; therefore, the fringe frequency of the optical pattern is aimed to be increased with this technique. This can be done with optical elements like lenses but fringe frequency would not be flexible, which is needed for test objects with different dimensions. Instead of using and changing lenses to have a suitable fringe pattern frequency, we propose a method that is simple to apply in Lloyd's mirror assembly, which relies on the method of changing the separation between the mirror and the fiber.

To be able to control the distance between the mirror and the fiber tip, there is a micrometer stage attached to the fiber chuck that holds the fiber. As in the the Young's Double Slit Experiment, changing the separation between the fiber and the mirror is similar to changing the slit separation. As a result of this change, the fringe pattern frequency can be varied easily. Then, the resultant pattern is projected on to a screen which includes a test object. In this way, micron scale measurements with flexible fringe pattern frequency are accomplished . The fiber optic Lloyd's mirror assembly and its modifications, which is used in our experiments, is sketched in Figure 3.1.

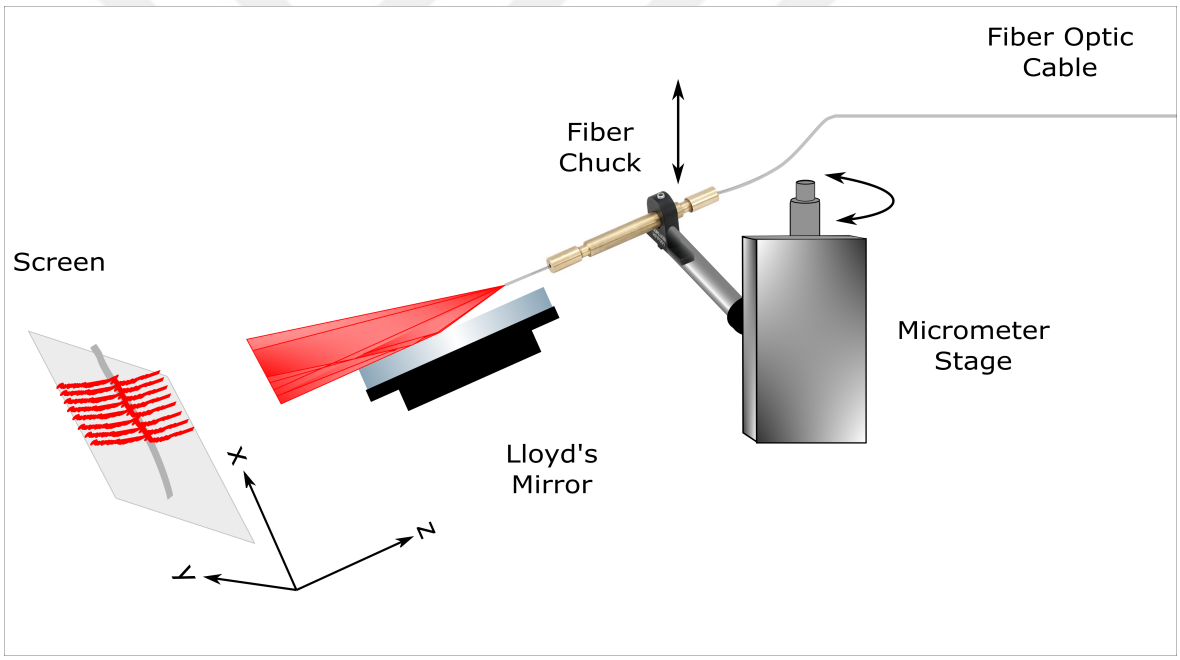

Figure 3.1. Modified fiber optic Lloyd's mirror assembly used in our experiments.

Example images of fringes with and without test objects that have different frequencies recorded using a microscope with a 10x magnification objective lens and a CCD camera are seen in Figure 3.2. To make the fringes more visible, a white correction fluid is used as a lacquer and the test object is a single mode fiber optic cable with partially stripped coating. The fiber has the diameters 245 μm and 125 μm with and without coating respectively. $\frac{d}{2}$ is the distance between the fiber and the mirror.

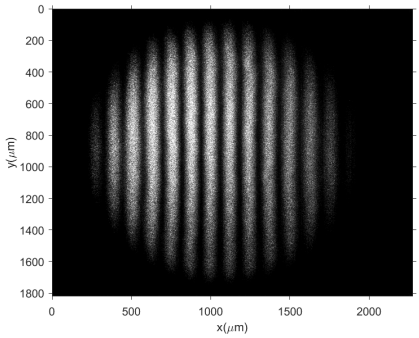

(a) $f_0 = 8.0\ mm^{-1}$, $\frac{d}{2} = 380\ \mu m$.

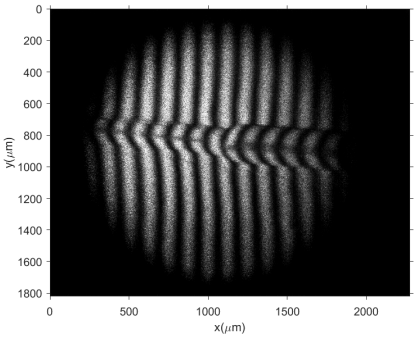

(b) $f_0 = 8.0\ mm^{-1}$, $\frac{d}{2} = 380\ \mu m$.

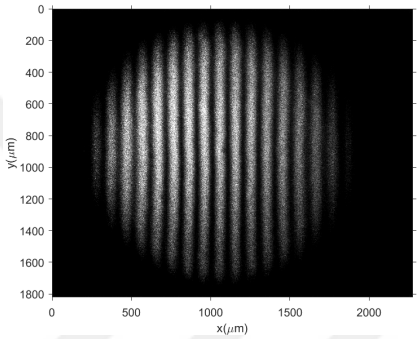

(c) $f_0 = 10.0\ mm^{-1}$, $\frac{d}{2} = 470\ \mu m$.

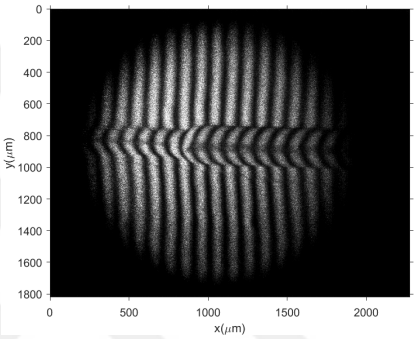

(d) $f_0 = 10.0\ mm^{-1}$, $\frac{d}{2} = 470\ \mu m$.

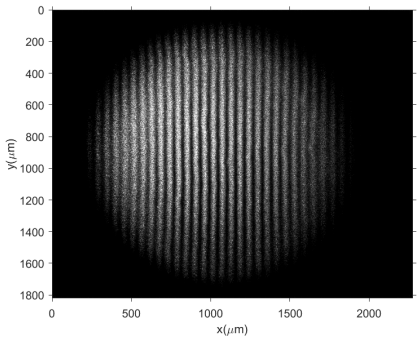

(e) $f_0 = 17.6\ mm^{-1}$, $\frac{d}{2} = 840\ \mu m$.

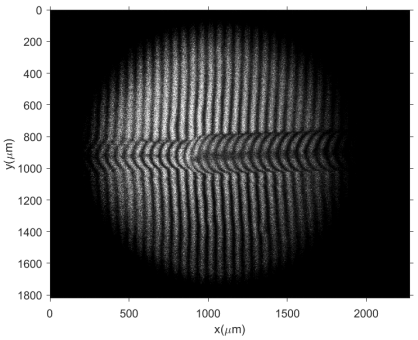

(f) $f_0 = 17.6\ mm^{-1}$, $\frac{d}{2} = 840\ \mu m$.

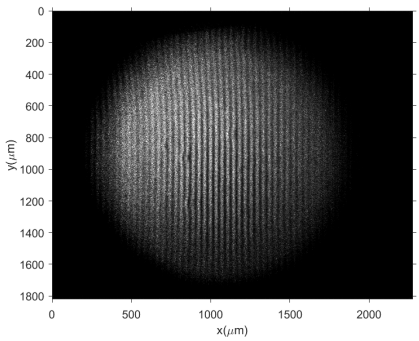

(g) $f_0 = 26.8\ mm^{-1}$, $\frac{d}{2} = 1300\ \mu m$.

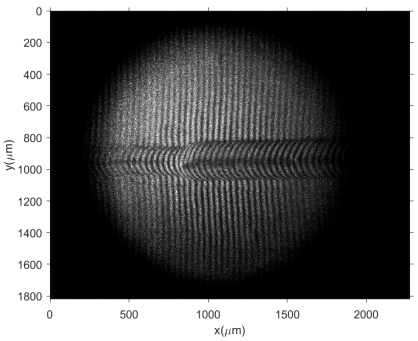

(h) $f_0 = 26.8\ mm^{-1}$, $\frac{d}{2} = 1300\ \mu m$.

Figure 3.2. Example fringes with and without a test objects in different frequencies.

As can be seen from Figure 3.2(g) and Figure 3.2(h), it is becoming difficult to differentiate fringes since the aberrations on the lens become more important as the frequency of the fringes increases. However, 1D CWT overcomes this problem and can identify the fringes nearly correct if the sinusoidal shape is preserved.

The whole experimental setup is sketched in Figure 3.3. The detailed, landscape version of the setup picture is given in Appendix A.

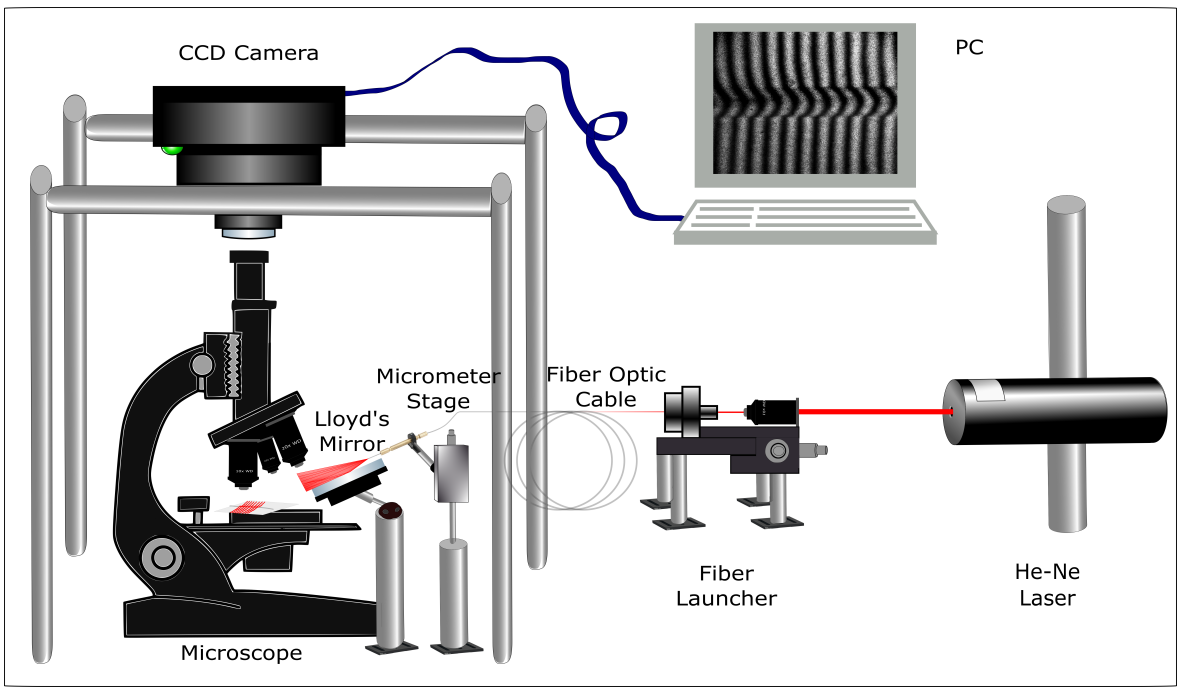

Figure 3.3. Our experimental setup.

3.1.2. Theory of Lloyd's Mirror

To extract the exact intensity function in this setup, we look Lloyd's mirror closely. As it is noticed from Equation 2.1, we need to find the phase difference $\Delta\Theta$ of two beams resulting from the path length difference. The construction is similar to the Young's double slit experiment as in Figure 3.4 except that a second light source does not exist in the Lloyd setup.

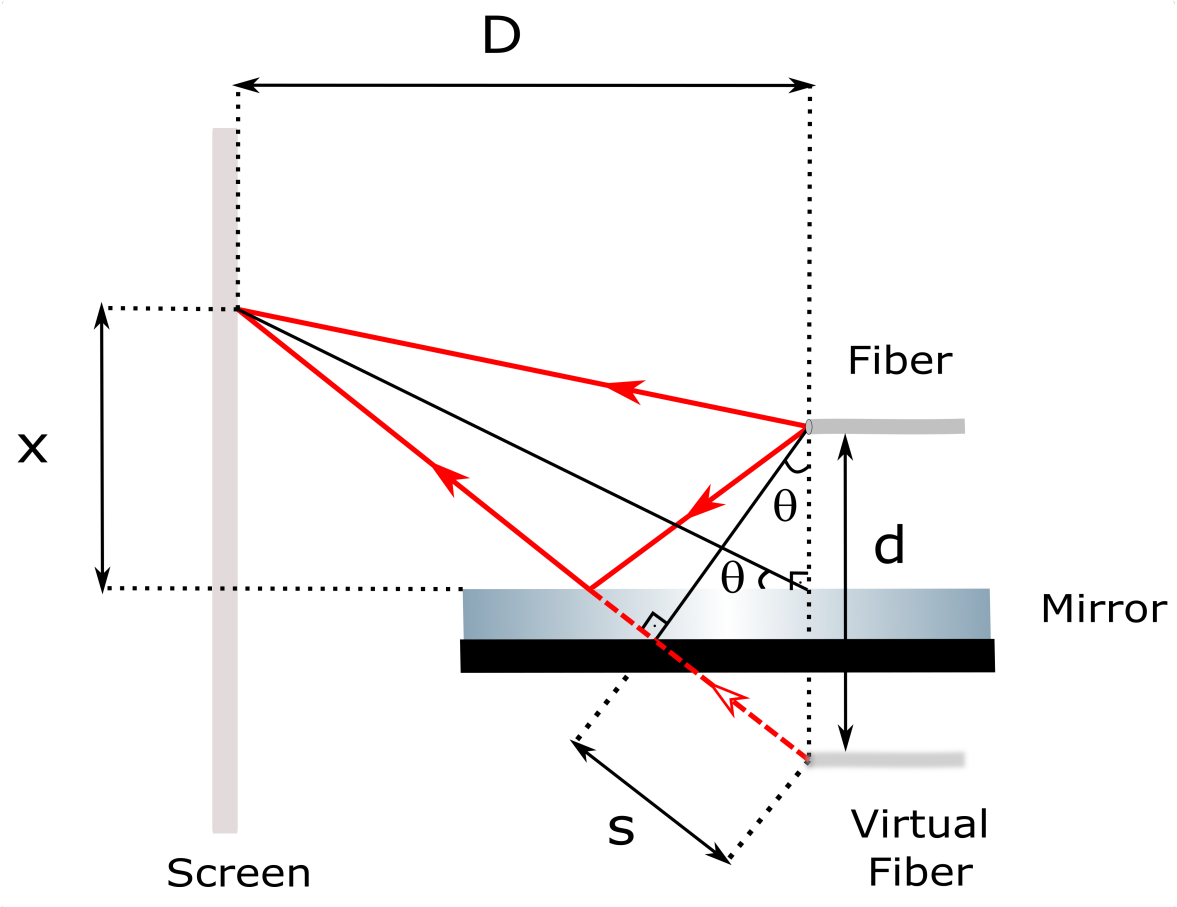

Figure 3.4. A close look to the Lloyd's mirror.

The second source is actually the image of the source in the mirror. To get the path length difference, we follow the same argument as in the Young's double slit and assume that the light that is reflected from the mirror comes from a different source, which is actually a virtual fiber. For an interference at a point on a screen that is x apart from the mirror axis and separated by a distance D from the fiber, we can draw a perpendicular line between the two beams (by assuming they are parallel) that gives equal paths on the left side and get the path length difference s as in the figure since d is the distance between the fiber and the virtual fiber and is small compared to D. Thus, $s \approx d \sin\theta$ is obtained. Since a λ difference in path length corresponds to 2π in phase difference, we multiply s with $\left(\frac{2\pi}{\lambda}\right)$. Also by using the fact that the second beam is reflected from a mirror, there is a phase difference of π between the two beams because of reflection from a denser medium. Since we have similar triangles

and $\sin\theta \approx \theta \approx \tan\theta$ for small θ, we can write the intensity function by adding every row (y axis) and the height related phase distribution like in [60] as follows

$$I(x,y) = I_0(x,y)\left[1 + V(x,y)\cos\left(\frac{2\pi dx}{\lambda D} + \pi + \phi(x,y)\right)\right] \tag{3.1}$$

The term $\frac{d}{\lambda D}$ is approximately equal to the fringe frequency f_0 while neglecting the effect of the projection angle. $D = 15cm$, $\lambda = 632.8nm$. From this term, the distance between the mirror and the fiber is calculated, which is half of d from the symmetry and is given for every frequency in Figure 3.2. It is also seen that increasing the distance d using the micrometer stage in our setup gives us a higher fringe frequency and consequently smaller fringes.

The last figure, Figure 3.1 and Figure 3.3 are prepared in Inkscape using this package [61].

3.2. Analysis of Projected Fringe Patterns

Since fringe patterns at micron scale is generated by the modified fiber optic Lloyd's mirror technique, it is doable to extract height distribution of test objects at micron scale.

To do that, firstly, the phase of the deformed fringes is extracted by using 1D CWT with Morlet Wavelet as the mother wavelet. The phase is wrapped between $-\pi$ and π due to the nature of the arctangent function so an unwrapping algorithm is applied. After that, the $2\pi f_0$ term is removed with a linear and a nonlinear carrier removal techniques to have a continuous phase map of the test objects. Then, a calibration technique is applied to relate the phase map of the object to its height distribution.

3.2.1. Phase Extraction with 1D CWT Using Morlet Wavelet

In 1D CWT, using morlet wavelet as the mother wavelet in Equation 2.16 is the most commonly used mother wavelet [62] since it is localized in both position and frequency spaces. Localization in position and frequency space is accomplished by gaussian envelope and complex exponential as seen in Equation 3.2 for the morlet wavelet.

$$\psi(x) = \pi^{-\frac{1}{4}} e^{icx} e^{-\frac{x^2}{2}} \tag{3.2}$$

To satisfy the admissibility condition in Equation 2.19, usually c is chosen 5 or 6 [46]. $c = 6$ is taken in our experiments. Real and imaginary parts of the morlet wavelet when c is chosen 6 are shown in Figure 3.5 [63].

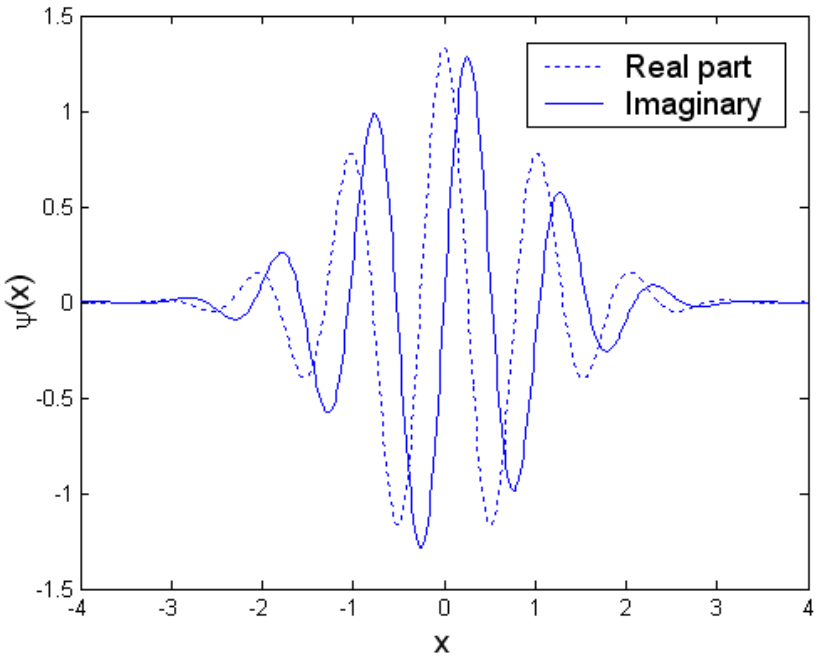

Figure 3.5. Imaginary and real parts of the morlet wavelet [63].

The Fourier transformations of both the intensity and the morlet wavelet function is used as in Equation 2.25 for faster computing. Fourier transform of the morlet wavelet is

$$\begin{aligned}\mathcal{F}(\psi(x)) = \hat{\psi}(g) &= \int_{-\infty}^{\infty} \psi(x) e^{-i(2\pi g x)}\, dx \\ &= \int_{-\infty}^{\infty} \left(\pi^{-\frac{1}{4}} e^{icx} e^{-\frac{x^2}{2}}\right) e^{-i(2\pi g x)}\, dx \\ &= \pi^{-\frac{1}{4}} \int_{-\infty}^{\infty} e^{-\frac{x^2}{2}} e^{-ix(2\pi g - c)}\, dx\end{aligned} \tag{3.3}$$

By merging the two exponential functions, using the variable change $k = 2\pi g - c$ and completing the square, gives us

$$\begin{aligned}\hat{\psi}(k) &= \pi^{-\frac{1}{4}} \int_{-\infty}^{\infty} e^{-\left(\frac{x^2}{2} + ikx\right)}\, dx \\ &= \pi^{-\frac{1}{4}} \int_{-\infty}^{\infty} e^{-\left[\left(\frac{x}{\sqrt{2}} + \frac{ik}{\sqrt{2}}\right)^2 + \frac{k^2}{2}\right]}\, dx \\ &= \pi^{-\frac{1}{4}} e^{\frac{-k^2}{2}} \int_{-\infty}^{\infty} e^{-\left(\frac{x}{\sqrt{2}} + \frac{ik}{\sqrt{2}}\right)^2}\, dx\end{aligned} \tag{3.4}$$

And by the variable change of $\left(\frac{x}{\sqrt{2}}\right) = t$, $dx = \sqrt{2}dt$, we get

$$\hat{\psi}(k) = \pi^{-\frac{1}{4}} e^{\frac{-k^2}{2}} \sqrt{2} \int_{-\infty}^{\infty} e^{-\left(t + \frac{ik}{\sqrt{2}}\right)^2}\, dt \tag{3.5}$$

The integral in Equation 3.7 is equal to $\sqrt{\pi}$ for $k < 0$ by using *Cauchy's theorem* [64]. If we put the value of the integral and change the variable k back, we get:

$$\hat{\psi}(g) = \pi^{-\frac{1}{4}} e^{\frac{-(2\pi g - c)^2}{2}} \sqrt{2}\sqrt{\pi} \tag{3.6}$$

Arranging the terms give us the same formula as in [37] which is

$$\hat{\psi}(g) = \frac{\sqrt{2\pi}}{\sqrt[4]{\pi}} e^{\frac{-(2\pi g - c)^2}{2}} \tag{3.7}$$

The only difference is the 2π term next to the g which comes from the definition of the Fourier transform.

From the FT analysis in review part, we have the Fourier transform of our intensity function in 1D which is

$$\hat{I}(g) \approx I_0(b)\delta(g) + \frac{I_0(b)V(b)}{2} e^{i(\pi+\phi(b))}\delta(g - f_0) + \frac{I_0(b)V(b)}{2} e^{-i(\pi+\phi(b))}\delta(g + f_0) \tag{3.8}$$

We have used the fact that I_0, V and ϕ are very slowly changing functions compared to $2\pi x$ term so that it can be approximated to constants, which are the first terms in Taylor expansion of them around b since b here is a point in the x axis.

If Equation 3.8 and Equation 3.7 are put into Equation 2.25 and the fact that $\hat{\psi}(ag) = 0$ when $g \leq 0$ is used (automatically terminates the first and the last terms in Equation 3.8, since the dirac delta function at $g = -f_0$ and $g = 0$ makes $\hat{\psi}(ag)$ zero and just $g = f_0$ case is left) , the following equation is obtained as our 1D CWT for one row of the analysed image:

$$\mathcal{W}(a, b) = \sqrt{a} e^{i(2\pi f_0 b + \pi)} \frac{\sqrt{2\pi}}{\sqrt[4]{\pi}} e^{\frac{-(2\pi a f_0 - c)^2}{2}} \frac{I_0(b)V(b)}{2} e^{i\phi(b)} \tag{3.9}$$

In the review part, we have mentioned that the phase of the wavelet transform at ridge points a_r is the same as the phase of a row of the intensity signal. So we find the maximum a_r values for every b value (particular column for a pixel) in the 2D array $\mathcal{W}(a, b)$, then the phase of the 1D ridge array $\mathcal{W}_r(a_r, b)$ is obtained using Equation 2.28. This gives us

$$\begin{aligned}\mathcal{P}_{wr}(a_r(b),b) &= arg(\mathcal{W}_r(a_r(b),b)) \\ &= \arctan\left(\frac{Im(\mathcal{W}_r(a_r(b),b))}{Re(\mathcal{W}_r(a_r(b),b))}\right) = 2\pi f_0 b + \pi + \phi(b)\end{aligned} \tag{3.10}$$

This is the wrapped phase map of the carrier frequency $2\pi f_0$ and the height distribution ϕ together. This analysis is done with the help of a personal computer firstly by taking the image of the deformed fringe patterns using a microscope and a CCD camera as shown in our setup in Figure 3.3. Then, the Fourier transform of every row is taken and put into 1D CWT algorithm in Matlab [65]. The algorithm uses the Fourier transformed 1D signal given and the Fourier transform of the morlet wavelet in Equation 3.7 to take the integral of them. After this operation, the 2D array in Equation 3.9 for a row of the image is acquired. The ridge arrays are found by looking at the maxima of the modulus of the 2D array like in Equation 2.26 as stated in [51], then, the positions of the ridges are selected from the phase array in Equation 2.28. After repeating this process for every row of the image, we have the last term in Equation 3.10, which is a wrapped phase of $2\pi f_0 x + \pi + \phi(x, y)$ due to the nature of the arctangent function. π is eliminated simply by subtraction. An example of a recorded image with our setup and the extracted wrapped phase using our own Matlab code is shown in Figure 3.6. The fiber optic cable laid down on a coverslip and correction fluid is applied to make fringes smooth and visible.

From Figure 3.6(c) and Figure 3.6(d), it is seen that there are 2π jumps between $-\pi$ and π in x axis due to the nature of the arctangent function. By using one of the unwrapping algorithm methods like in [66] or in [67], the continuous distribution of $2\pi f_0 x + \phi(x, y)$ is obtainable. A code for Matlab can be found here [68] or here [69] for the corresponding methods respectively. Both of them are used since the last one is fast but averaging the resultant phase in z axis where as the first one is slow but giving the actual phase values. By applying one of the unwrapping algorithms to the wrapped phase in Figure 3.6, the continuous phase map is obtained as in Figure 3.7.

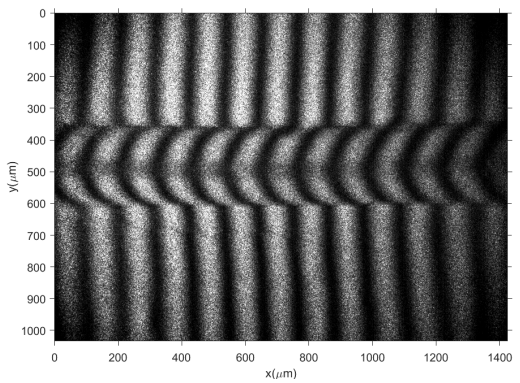

(a) Recorded and cropped image.

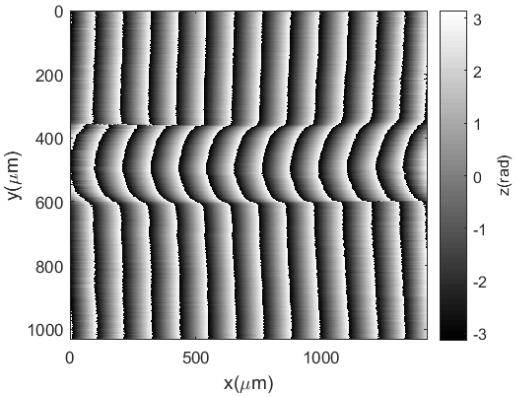

(b) Wrapped phase map viewed from the top.

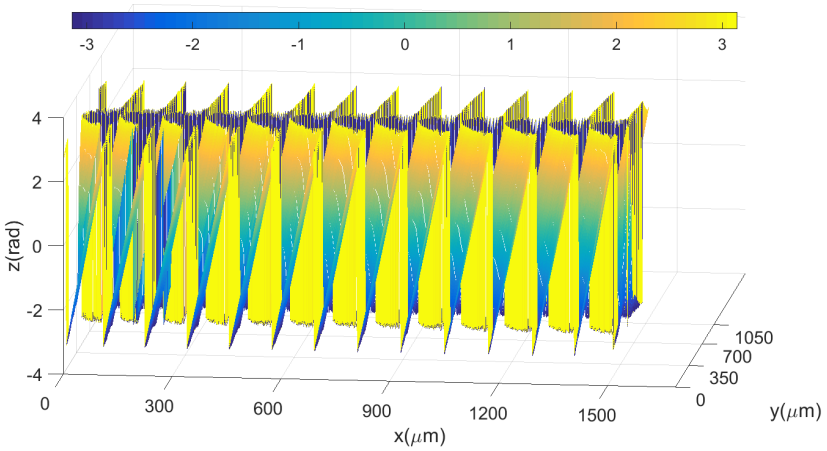

(c) Wrapped phase map viewed from the side.

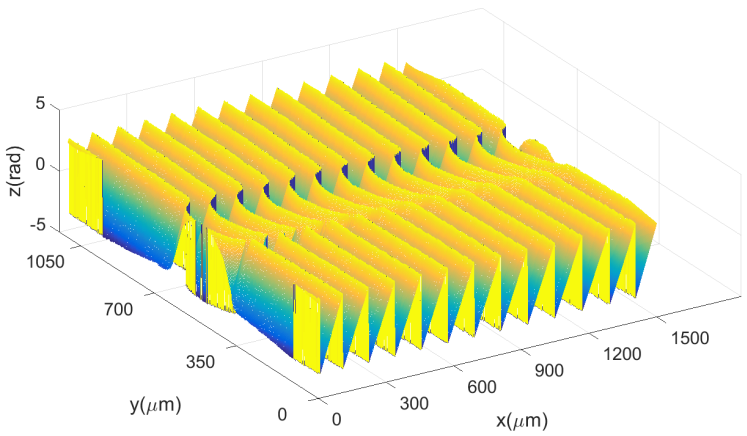

(d) Wrapped phase map in 3D.

Figure 3.6. Wrapped phase of a fiber optic cable with thickness of around 245 μm.

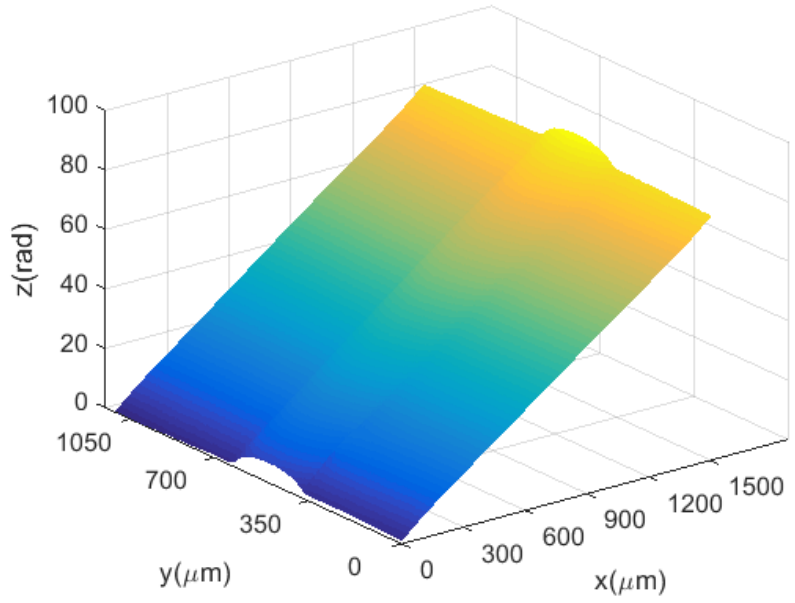

(a) Viewed at azimuth angle −37.5, vertical elevation at 30 degrees.

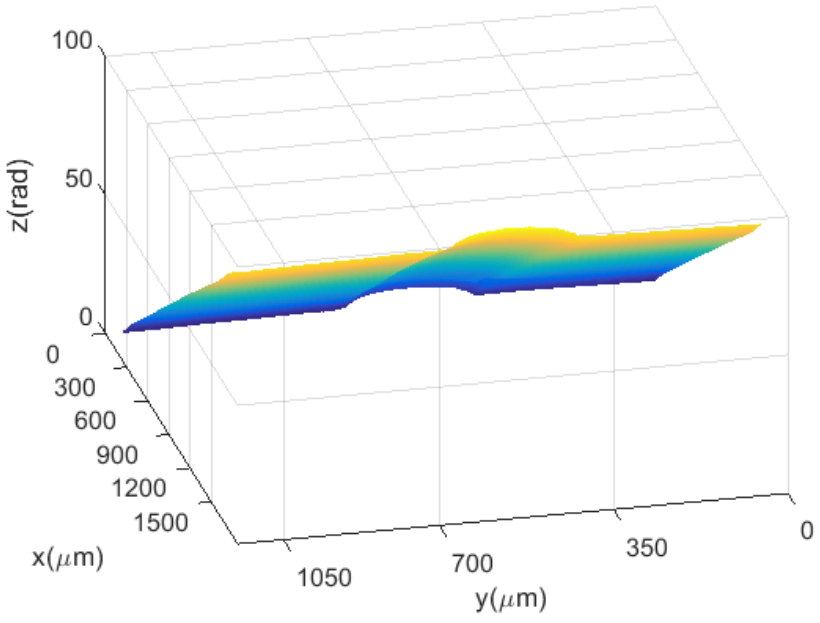

(b) Viewed at azimuth angle −76.5, vertical elevation at −38 degrees.

Figure 3.7. Unwrapped phase of a fiber optic cable with thickness of around 245 μm viewed from different angles.

3.2.2. Carrier Frequency Removal

After the continuous phase map is obtained as in Figure 3.7, the carrier $2\pi f_0$ has to be removed to get the object related phase distribution $\phi(x, y)$. Carrier removal of the previous test object, which is a fiber optic cable with thickness around 245 μm is shown in this subsection.

As mentioned before in the review chapter, there are many techniques for carrier frequency removal. We shall use both a linear and a nonlinear carrier removal techniques. In linear carrier removal, we assume f_0 is constant in x and there is not a nonlinear term dependent on the x coordinate. Thus, a plane fit is done to a portion of our phase map that does not involve object related phase and the resultant plane with inclination $2\pi f_0$ is subtracted from our phase map. By doing this, just a height related phase is obtained. In nonlinear carrier removal, reference subtraction method is used, which additinally consists of a separate recording of the flat surface plane on which the test object is laid down. In this method, whatever term exists in the fringe signal is subtracted from the phase map and again just height related phase distribution of the test object is obtained. Both results are compared and it is investigated that whether the carrier frequency f_0 is x dependent or not.

For the plane fit method, $ax + by + c$ is used as the fitting function. The fit in y direction is not necessary but since it fits to the surface plane beneath the test object, it eliminates possible slope errors in y axis of the microscope stage. Then, the plane extracted from the fit is extended to the size of the phase map for pixelwise subtraction. After the subtraction of the fitted plane from the phase map, pure object phase is obtained. The region used for the plane fit on the image, resultant plane after fit with its parameters (notice that b is very small) and the object phase map after the subtraction of the plane from the phase map in Figure 3.7 are shown in Figure 3.8.

For the reference subtraction method, two images are required. One of them is the same image with the test object on the previous method and the other is an image recorded without the test object, which is called the reference image. Unwrapped

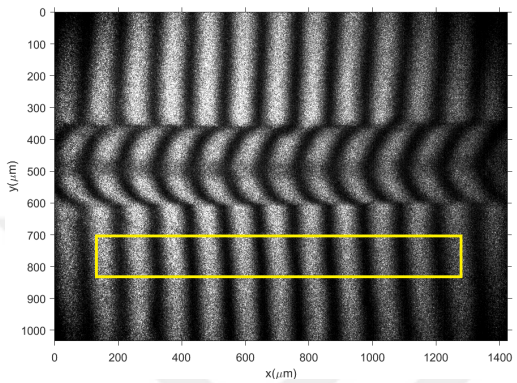

(a) Selected flat region for plane fitting.

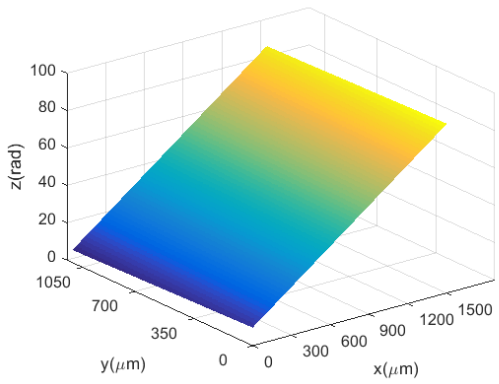

(b) Plane extracted from the fit with paramters $a = 0.1008$, $b = -0.004947$, $c = 9.706$.

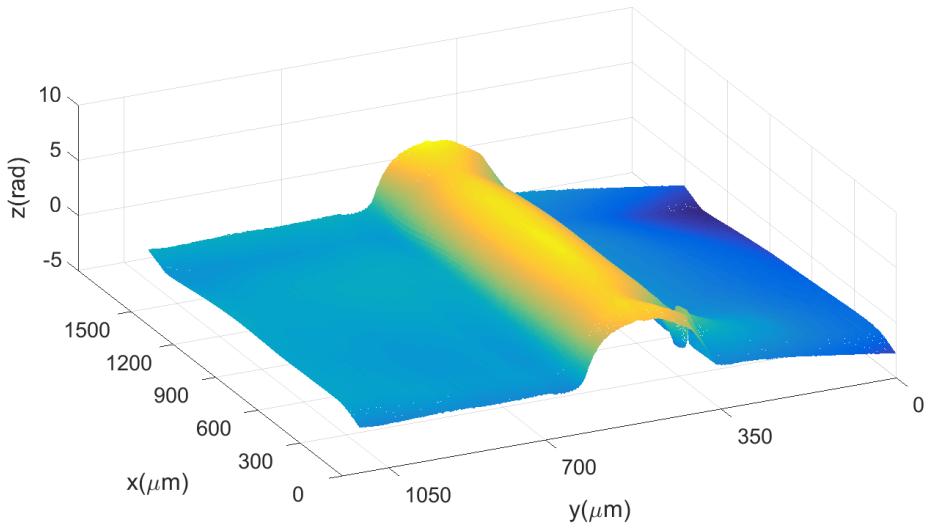

(c) Object phase map after the subtraction.

Figure 3.8. Carrier removal with plane fitting.

phase of the two images is extracted with the method mentioned previously. Then, the unwrapped phase of the reference image is subtracted from the unwrapped phase of the image with the test object. In this method, any nonlinear term that is not related with the test object is eliminated. The reference image is recorded by sliding the coverslip on the microscope stage and capturing a position on it without the test object. Reference image, its unwrapped phase and the pure object phase is shown in Figure 3.9.

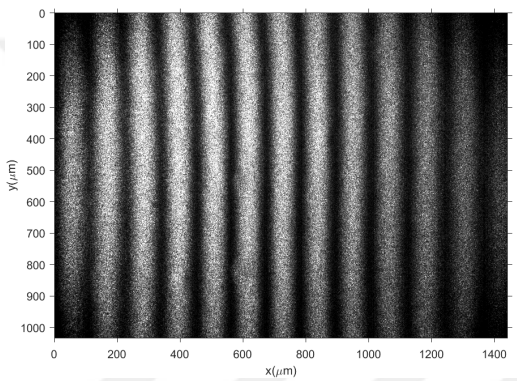

(a) Reference image.

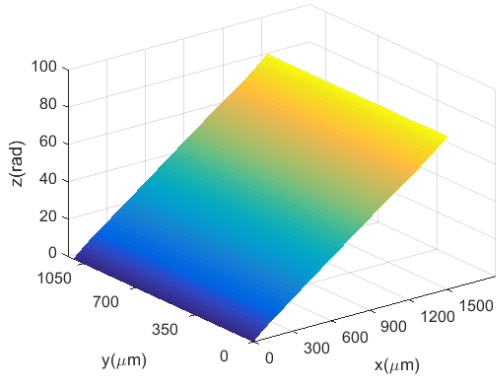

(b) Unwrapped phase of the reference image.

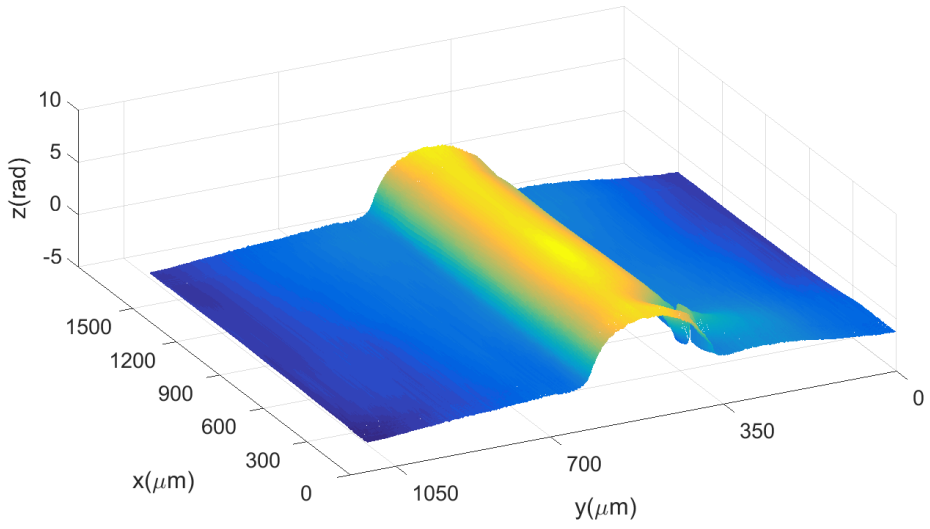

(c) Object phase map after the subtraction.

Figure 3.9. Carrier removal with reference subtraction.

At some areas like the edges of the image and at the back of the fiber optic cable, we see flatter and smoother transitions in the reference subtraction method than the plane fitting method. The reason behind this is that, the selected region for the plane fit in Figure 3.8(a) is bent differently than the upper region in the same figure. A correction fluid is used as a lacquer and it gets thicker on the regions close to the fiber. As a result of that, while the lower region has an increasing height profile in increasing y towards the fiber, the upper region has a decreasing height profile away from the fiber. It is obvious that fitting a region like this and subtracting it from the whole image cause that region to be flat while making the other regions unreliable. It is seen with a comparison of the profiles of Figure 3.8(a) and Figure 3.9(a) as in Figure 3.10.

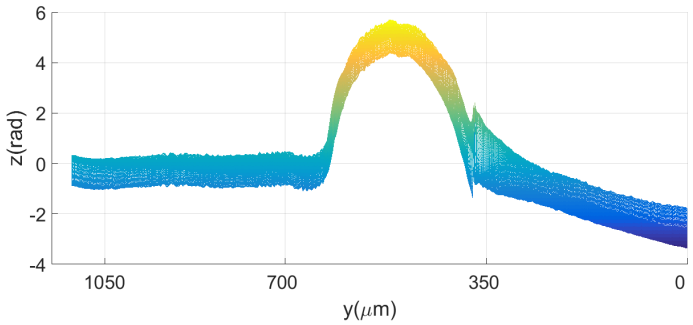

(a) Profile in plane fitting method.

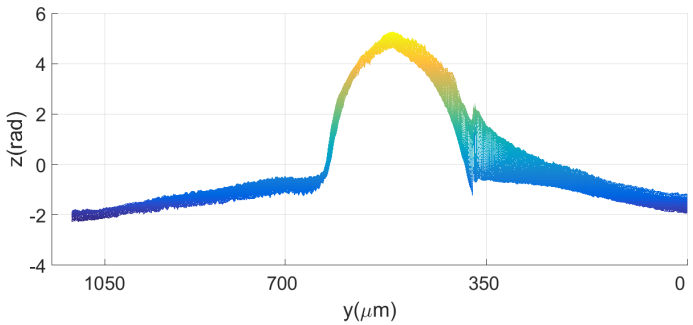

(b) Profile in reference subtraction method.

Figure 3.10. Comparioson of the fiber phase profiles extracted with the two carrier removal methods.

As stated in [52], reference subtraction method is slower since it requires a reference image additional to the image with a test object. It also doubles the uncertainty of phase values since it is randomly distributed on the phase values of both images. Addition or subtraction of them increase the uncertainty. Plane fitting method is more reliable than the reference subtraction method if there are no nonlinear terms since the captured reference image may not be the same as the plane under the test object due to various reasons like having different thickness. However, in our case, eventhough we do not know whether we have nonlinear terms in our fringes or not, correction fluid used for fringe visibility make the use of plane fitting method unreliable for us. So it is continued with the reference subtraction method for carrier removal since correction fluid is used in our experiments with fibers and to guarantee the removal of the possible nonlinear terms in our fringe patterns. At the end, its thickness for a correction is discussed at the end of this chapter.

3.2.3. Phase to Height Conversion

At the end, all that remains is to turn this retrieved phase map of the test object to a height distribution. The most commonly used method is the triangulation one, which is depicted in Figure 3.11 [70].

Fringe patterns are made parallel to y axis. If there is no object on the screen, light coming from the point P falls onto the screen at point B. The image at B is received at point C' by the camera. However, if there is an object like the one in the figure, the light coming from P falls onto the object surface at point E. This point is captured by the camera at point C. So there will be a fringe shift from B to A in the presence of an object with height h at that point. This physical shift of distance $\overline{AB}$ is equal to the received shift $\overline{CC'}$ by the camera. The similarity between the triangles $\Delta ABE \sim \Delta CPE$ is used to write

$$\frac{\overline{AB}}{\overline{EA}} = \frac{\overline{CP}}{\overline{EC}} \tag{3.11}$$

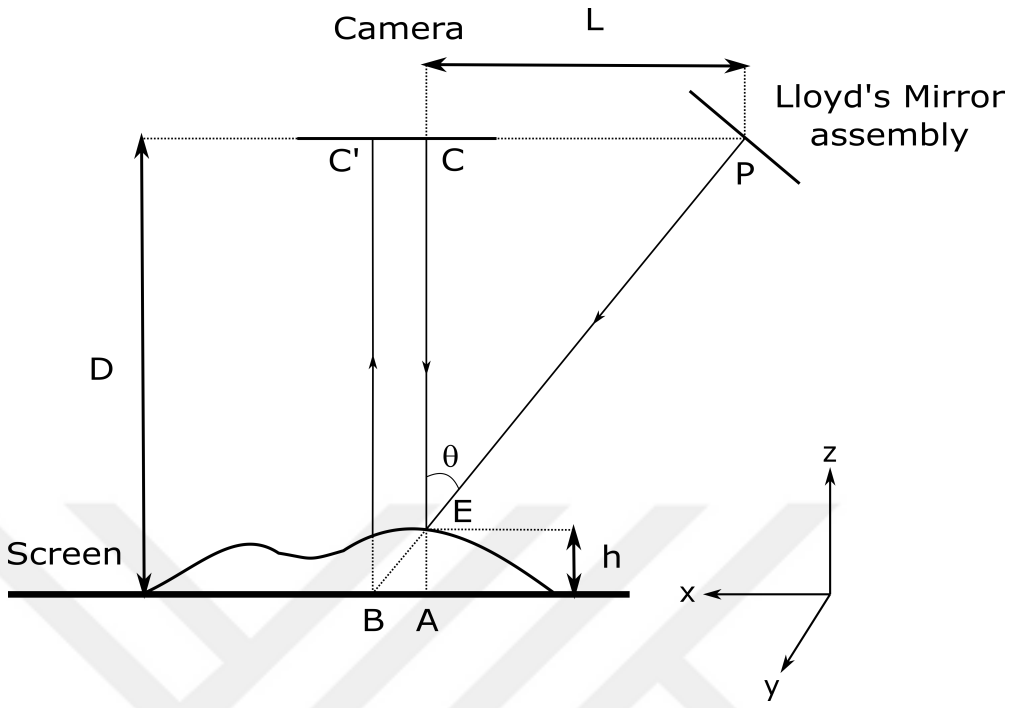

Figure 3.11. Triangulation method for phase to height conversion [70].

If $\overline{EA} = h$, $\overline{EC} = D - h$ and $\overline{CP} = L$ is used, we get

$$\frac{\overline{AB}}{h} = \frac{L}{D-h} \tag{3.12}$$

Then, by arranging the terms, the height h is obtained as

$$h = \frac{\overline{AB}\ D}{\overline{AB} + L} \tag{3.13}$$

Extending h and $\overline{AB}$ at ever point on the surface in x direction gives

$$z(x) = \frac{\delta(x)D}{\delta(x) + L} \tag{3.14}$$

where $z(x)$ is the height h, $\delta(x)$ is the shifted distance $\overline{AB}$ that corresponds to the object surface at any x point.

The relation between shifted distance and the phase shift is needed. A wavelength λ_0 shift of fringe patterns on the screen is equivalent to a phase shift of 2π and the shifted distance $\delta(x)$ is equal to the phase shift of $\phi(x)$. Since they are proportional, we can write

$$\delta(x) = \frac{\phi(x)\lambda_0}{2\pi} \tag{3.15}$$

where $\phi(x)$ is the phase difference between the phase of the fringes on the reference plane and on the object surface. Also λ_0 is the wavelength of the projected fringe pattern and is equal to $\frac{1}{f_0}$. If we substitute f_0 and $\delta(x)$ in Equation 3.15 into Equation 3.14 by neglecting the $\delta(x)$ in the denominator since $D \gg \delta(x)$, phase to height conversion formula is obtained as

$$z(x, y) = \frac{\phi(x, y)D}{2\pi f_0 L} \tag{3.16}$$

Here the axis y is also included in z since the parameters L, D are constants and as previously mentioned, $\phi(x, y)$ can be extracted for every y pixel by adding consecutive $\phi(x)$ values.

After phase extraction, the accuracy of the height in Equation 3.16 depends on the uncertainties of the measurements for the parameters L, D, and f_0. In [71], the fact that $\frac{L}{D}$ is equal to $\tan(\theta)$ with the previous approximation $D \gg \delta(x)$ is used to estimate the parameters accurately. Instead of measuring L and D directly, they use a calibration method that raises the microscope stage step by step with known increments and find the angle θ that minimizes the error of the expected step heights. Additionally, it is harder to measure L and D in our setup because the camera and the

Lloyd's mirror assembly are not aligned in the z axis as seen in Figure 3.3. One needs to track the position of the camera lens on the level of fiber optic cable and remove the objective lenses on the microscope to measure D, which can change the parameters upon remounting.

Instead, since it is known that $z(x, y)$ and $\phi(x, y)$ are related with a constant c_0 as stated in [72], a calibration method is used as in the paper that θ is optimized, but to find the constant in front of $\phi(x, y)$ that relates to $z(x, y)$ instead of θ as in [73].

After the microscope stage is set by using the coarse adjustment knob on one side of the microscope for the best position ensuring that the flat plane on the stage is on the focal plane of the $10X$ objective lens by looking the fringe patterns on the computer screen, we take some number of images like 16 while increasing the stage with 10 μm steps using the fine adjustment knob that is mounted on the coarse adjustment knob. The fine adjustment knob has 1 μm resolution. Then, five consecutive portions cropped from selected five images are merged in one image to study the step heights. Phase extraction of an image constructed by cropped images from five 20 μm steps is shown in Figure 3.12. Image with 0 μm height is used as the reference image. For once, five images are chosen and used to determine the conversion coefficient, then, the test objects are measured without a new calibration unless the microscope stage requires to be moved with the coarse adjustment knob to focus on the new test objects with different heights.

Since we crop and paste images with different heights, our steps are not continuous. This can cause phase ambiguities. Beyond the height difference that causes π phase shift, it cannot be differentiated whether we increased the height and shift the fringes left or decreased it and shift the fringes right. In situ, visual inspection while increasing the microscope stage slowly, one can determine the height difference in two images that causes π phase shift by looking at the crests and troughs of the fringe intensities in both images. If a crest of the fringe intensity in one image is matched with a trough of the fringe intensity in the other image, this means that the height difference between the two images corresponds to a phase change of π and must not be

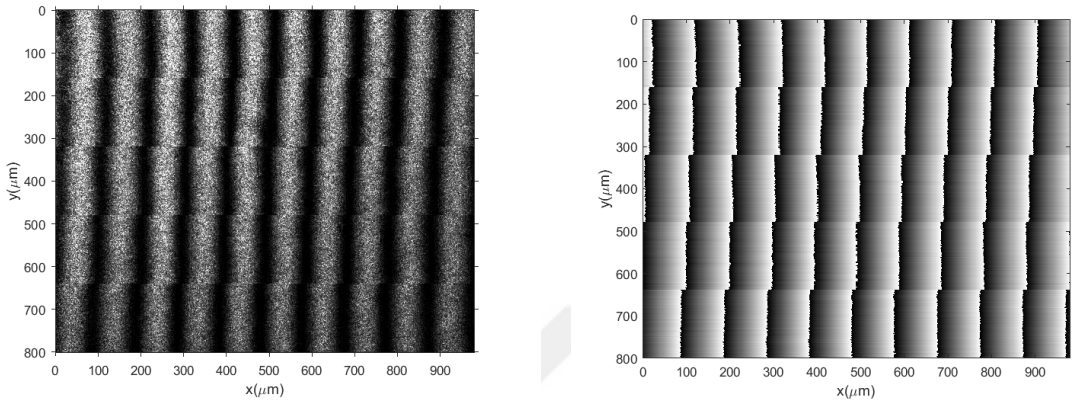

(a) Constructed image from five images (from top to bottom cropped images at 0,20,40,60,80 μm).

(b) Wrapped phase map of the constructed image.

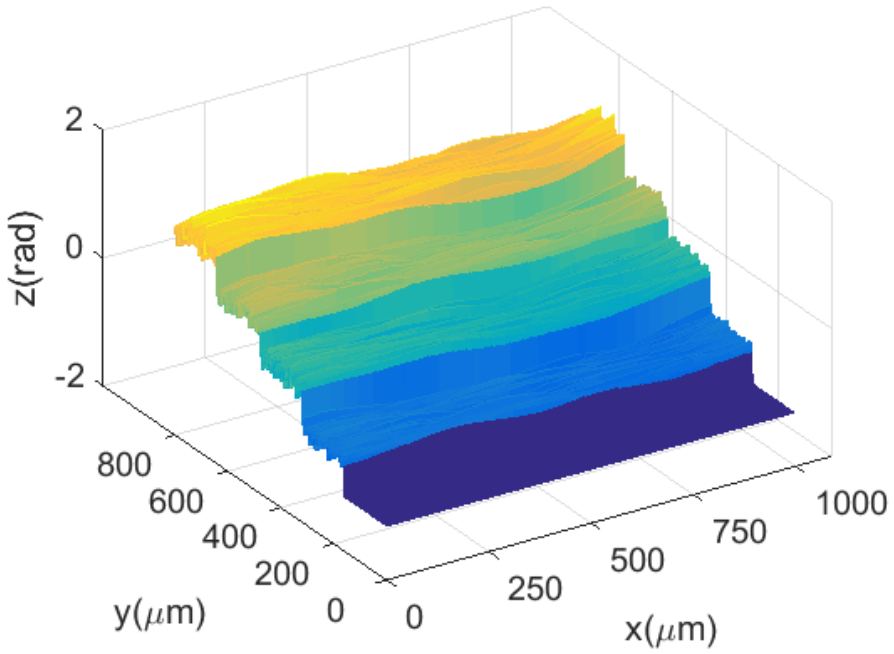

(c) 3D phase map of the constructed steps.

Figure 3.12. Phase extraction of five steps for calibration, consecutively having 20 μm difference between them.

exceeded when choosing consecutive steps for calibration. In Figure 3.13, we showed two images with phase difference larger than π including respective stage heights of them and five steps that involve those two images to show the phase ambiguity. For continuous test objects that have no height jumps between consecutive pixels larger than this value, we do not have these ambiguities.

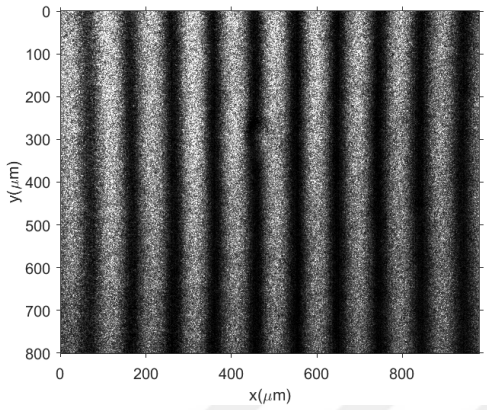

(a) Stage at 0 μm.

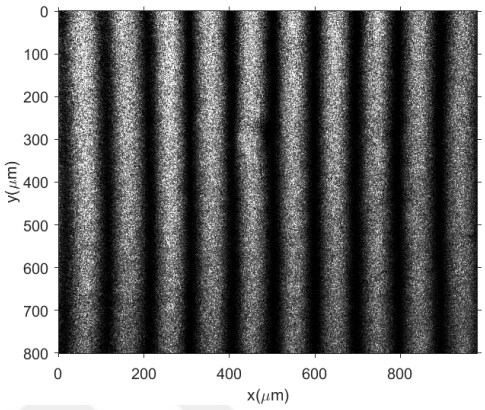

(b) Stage at 110 μm.

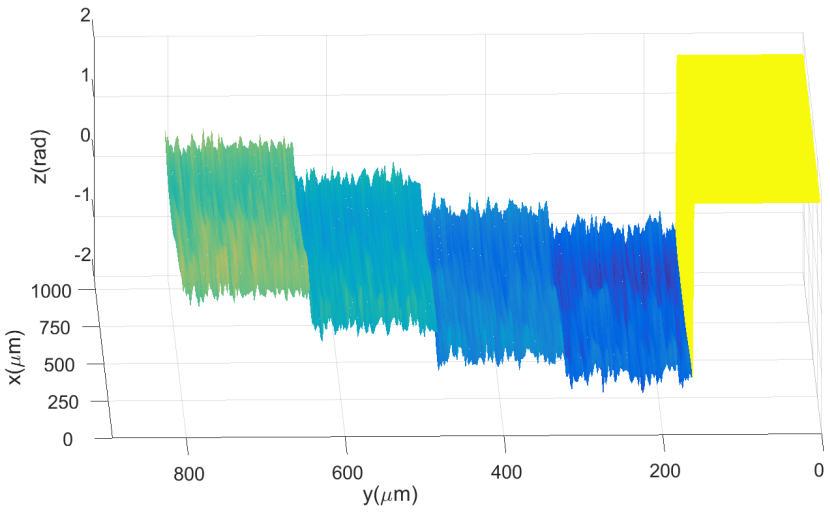

(c) 3D phase map of steps 0,110,120,140,160 μm in increasing y.

Figure 3.13. Height that starts phase ambiguities.

As seen from the edges of the images, we have approximately phase shift larger than π if images that have a difference of 110 μm is merged one after the other. Since the wrapped phase is between $-\pi$ and π and we do not know the fringe ordering between the two images, a jump larger than π in the phase map makes the phase to

be located at a lower level than the previous value as shown in Figure 3.13(c). Instead of making second step 110 μm higher than the first one, the code makes it around 100 μm lower. The other steps follow the correct differences but are not in the correct positions due to the previous false phase unwrapping.

There are new articles to solve this problem by determining the fringe order between two images as in [74]. However, they are not needed either in calibration or in object measurements since lower step values are enough for calibration and our test objects are continuous and smooth with the help of correction fluid.

Once the five steps with no phase ambiguities are obtained, the differences between these steps are analyzed. The data are fit with sums of Heaviside functions as in Equation 3.17 in Matlab.

$$\begin{aligned} z(x,y) = a\ heaviside(y-i) + b\ heaviside(y-2i) \\ + c\ heaviside(y-3i) + d\ heaviside(y-4i) + ex + f \end{aligned} \tag{3.17}$$

where a,b,c and d are the length of the heaviside functions which are consecutive step sizes and used as free parameters, i is a variable that represents the increment in the y axis that the images cropped with, e is for eliminating the possible small angle on the microscope stage and f is a constant that determines the intersection on the $y-z$ plane .

16 images with 10 μm steps are captured, and five images with 40 μm difference chosen starting from zero. Due to computational limitations, a portion of the phase map is used as our raw data to make the fitting. After fitting it with the function in Equation 3.17, the average of four height differences are taken which are given by a,b,c and d since the inclination is very small (e is around 0.0006). The reason for

not taking the weighted average is that height change implemented by moving the microscope stage does not cause an additional phase error and the sigma for the four parameters is the same and 0.002 *rad*. Fitting result is showed in Figure 3.14 where the raw data are in black and the function fitted to it is colored.

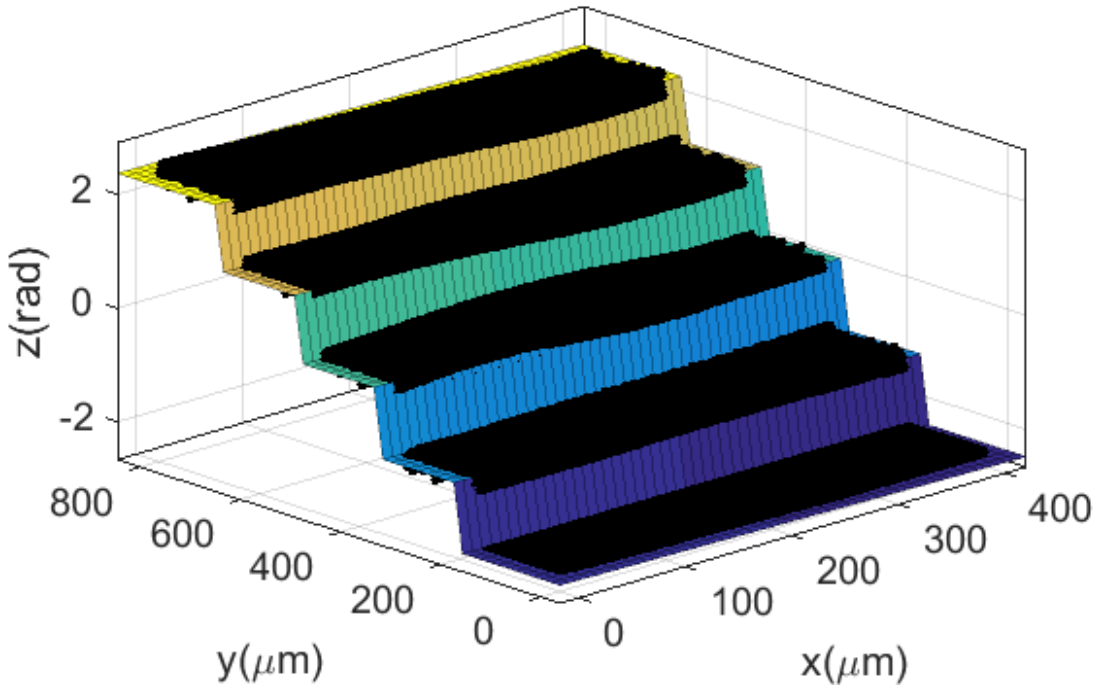

Figure 3.14. Fitting to the constructed phase map of 40 μm steps for calibration.

The fit parameters and their corresponding sigmas are as follows

$$\begin{aligned} a &= 1.199 \pm 0.002\ rad & b &= 1.220 \pm 0.002\ rad \\ c &= 1.161 \pm 0.002\ rad & d &= 1.133 \pm 0.002\ rad \\ e &= -0.0006208 \pm 0.0000110 & f &= -2.350 \pm 0.002\ rad \end{aligned} \tag{3.18}$$

By using the average and the error propagation formula in Equation 3.19, the corresponding phase p and its sigma for a 40 μm step are calculated.

$$p = \left(\frac{a+b+c+d}{4}\right)$$
$$\sigma_p = \sqrt{\left(\frac{\partial p}{\partial a}\sigma_a\right)^2 + \left(\frac{\partial p}{\partial b}\sigma_b\right)^2 + \left(\frac{\partial p}{\partial c}\sigma_c\right)^2 + \left(\frac{\partial p}{\partial d}\sigma_d\right)^2} \tag{3.19}$$

This gives us the phase value and its sigma for 40 μm as $p \approx 1.178 \pm 0.001\ rad$. To find the height corresponding to 1 rad, which is our calibration constant c_0, and its sigma, 40 μm is divided to p and error propagation for division is used as in Equation 3.20. Sigma for $40\mu m$ is ± 1 μm due to the precision of the fine adjustment knob of the microscope.

$$c_0 = \left(\frac{40\ \mu m}{1.178\ rad}\right) \approx 34\ \mu m/rad$$
$$\sigma_{c_0} = \sqrt{\left(\frac{1\ \mu m}{1.178\ rad}\right)^2 + \left(\frac{40\ \mu m \times 0.001\ rad}{(1.178\ rad)^2}\right)^2} \approx 1\ \mu m/rad \tag{3.20}$$

If the extracted phase map is multiplied with this value, the height distribution of a test objects is obtained as

$$z(x,y) = c_0 \times \phi(x,y) \tag{3.21}$$

By doing a constant surface fitting to any step in Figure 3.14, sigma of a radian is found to be 0.0016 rad. Since $c_0 = 34 \pm 1\ \mu m/rad$ is known, error on every single point on the phase map is found by the formula in Equation 3.22, which is extracted by doing an error propagation to Equation 3.21. $\phi(x,y)$ is in radians.

$$\sigma_{z(x,y)} = \sqrt{(0.0016\ rad \times 34\ \mu\ m/rad)^2 + (\phi(x,y) \times 1\ \mu m/rad)^2} \tag{3.22}$$

So the longitudinal calibration is done with the method above. The transversal calibration is easy and done by using a stripped fiber optic cable with thickness $125 \pm 1\ \mu m$. Our field of view is around $1.5\ mm^2$ for the rectangle images cropped for analysis.

3.3. Results and Discussions

Height distribution of a $245 \pm 15\ \mu m$ [75] fiber optic cable is extracted after all the procedures above are applied and is shown in Figure 3.15 with its maximum and minimum profiles. As can be seen from the cross sections, our maximum value is about two sigma away from the supplied height value of the fiber but minimum value is not close that enough. The average of the maxima on the all cross sections along the fiber is calculated and it is 216 μm. This value is 30 μm away from the accepted value.

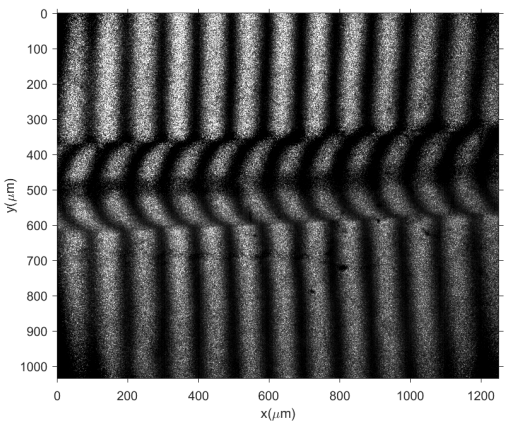

(a) Captured and cropped image.

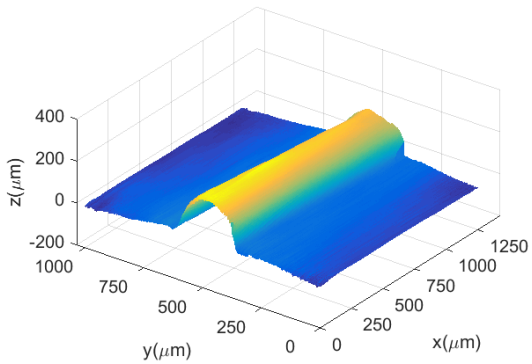

(b) 3D height distribution of the fiber.

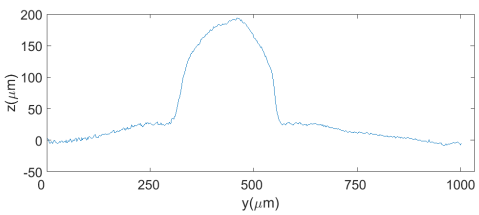

(c) Cross section with the minimum height, $194 \pm 6\ \mu m$.

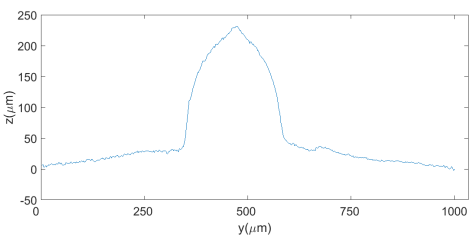

(d) Cross section with the maximum height, $231 \pm 7\ \mu m$.

Figure 3.15. Height distribution and cross sections of a $245 \pm 15\ \mu m$ fiber optic cable.

The reason behind this can be the correction fluid used on the fiber and on the coverslip. A line of shade can be noticed from the Figure 3.15(a), the correction fluid is absent on this shaded area, which are the peak points of the fiber, due to a possible flow with effect of the gravity before it dries and human factors like brushing direction. Also there is no correction fluid under the fiber because we applied the correction fluid when the fiber and the coverslip are in contact. Since we use reference subtraction as the carrier removal, the reference image has thicker correction fluid on its surface than on the fiber. As a result, we subtract an extra correction fluid thickness from the height of the fiber while subtracting the reference plane. So we should measure the average thickness of a layer of the correction fluid to be able to deduce whether this 30 μm difference is coming from this effect of the correction fluid or not.

To do this, correction fluid on a large area on a coverslip is applied. After waiting some time to dry it, another layer of correction fluid is applied on the half of the previously applied correction fluid. As a result, we have a step of one layer of correction fluid. The thickness of this step is studied using the same methods we have mentioned so far. The 3D height distribution and a cross section is given in Figure 3.16.

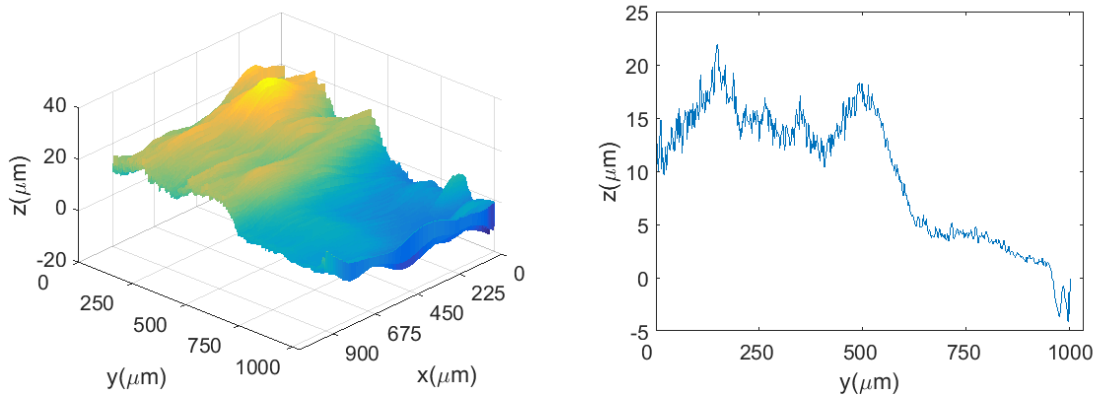

(a) Height distribution of the correction fluid layers.

(b) Crossection of the layers.

Figure 3.16. Height distribution and a cross section of the correction fluid layers.

The thickness of the step is around 15 μm but there are fluctuations from 5 μm to 20 μm which is around 15 μm. This layer thickness changes depending on effects like the

used brush and pressure of application and so on. As in [76], industrial primer coating has a thickness around 25.4 μm per coating layer, which has a similar ingredients as the correction fluid. This is enough to see the gap between our measurements and the expected value. However, additionally, it is better to look for the thickness of a correction tape since it will have less fluctuations and is more reliable than the correction fluid. It will not be affected by the brush type or human factors.

We use the same procedure as in the correction fluid but not on a coverslip since correction tape cannot stick to a coverslip and slides over it. One layer is applied on a flat, hard sheet of cardboard parallel to the y axis, then another layer of tape is applied vertically that is crossing the other tape in x axis. Than the transition from one lay to the other is studied. The height distribution and a cross section is given in Figure 3.17.

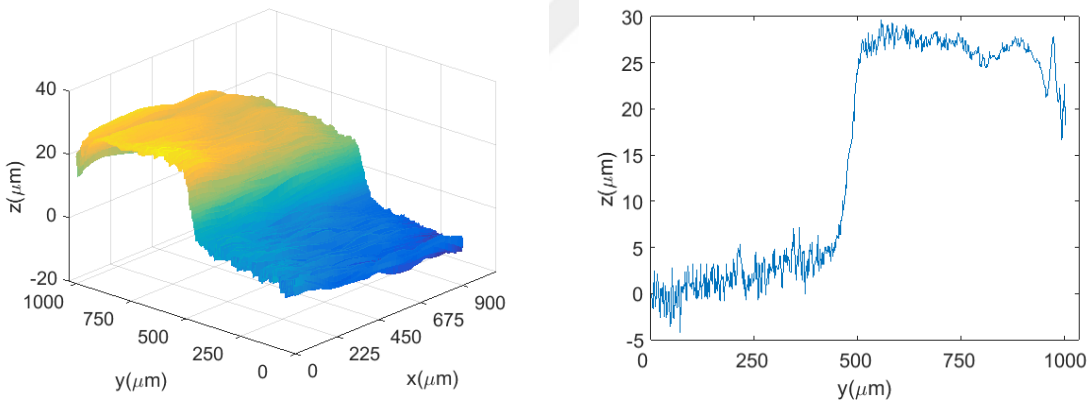

(a) Height distribution of the correction tape layers.

(b) Crossection of the layers.

Figure 3.17. Height distribution and a cross section of the correction tape layers.

Separate analysis of the two layers shows that they have a difference of 24 ± 2 μm. This is close to what is expected from our previous analysis and the online search.

For the measurement of a 170 ± 10 μm fiber optic cable, the effect of the correction fluid is also proved as before since the right side of the fiber has nearly no correction fluid at its peak points and this is seen as a shade of line on that area as in Figure 3.18(a) whereas the left side of it has no shaded areas on its peak. Captured image, the

height distribution and the cross sections from the left , heighest point and the right, lowest point is shown in Figure 3.18. The results are $160 \pm 5\ \mu m$ for the minimum value at the left side and $191 \pm 6\ \mu m$ for the maximum value at the right side. Consulting the given error for the fiber, our errors and the correction fluid thicknes and its fluctuation, our measurements are seemed to be in the desired range.

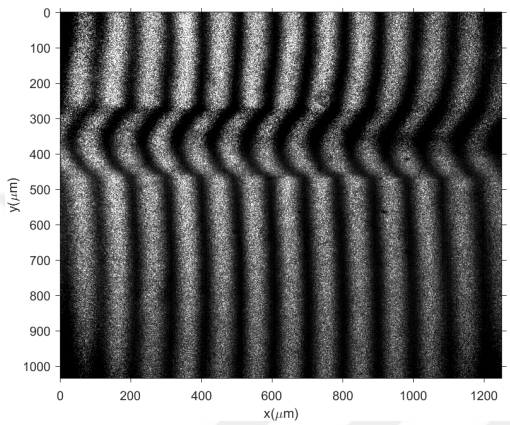

(a) Captured and cropped image.

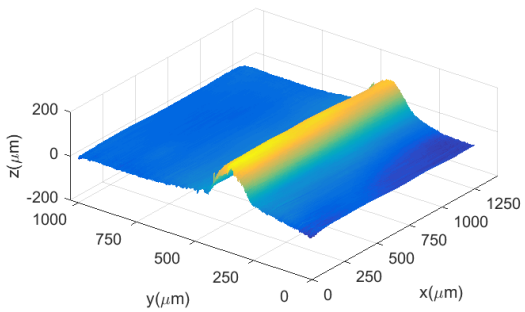

(b) 3D height distribution of the fiber.

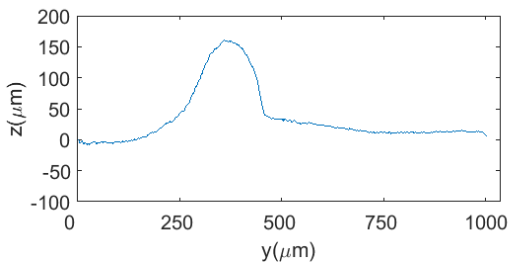

(c) Cross section of the right portion with the minimum height, $160 \pm 5\ \mu m$.

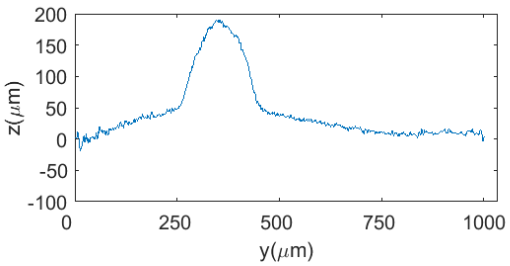

(d) Cross section of the left portion with the maximum height, $191 \pm 6\ \mu m$.

Figure 3.18. Height distribution and cross sections of a $170 \pm 10\ \mu m$ fiber optic cable.

The fiber with the thickness of $245 \pm 15\ \mu m$ has a coating around it for protection. There is cladding beneath the coating. If it is stripped with a fiber stripping-tool, the cladding has the diameter of $125 \pm 1\ \mu m$. Since it is centered on the same axis with the coating, our measurements give us sum of the thicknesses of the cladding diameter and the difference between the radius of the coating and the radius of the cladding, $185 \pm 5\ \mu m$ as sketched in Figure 3.19, using the error propagation for summation.

Captured image, height distribution and the cross sections for coating and cladding for the partially stripped fiber is illustrated in Figure 3.20.

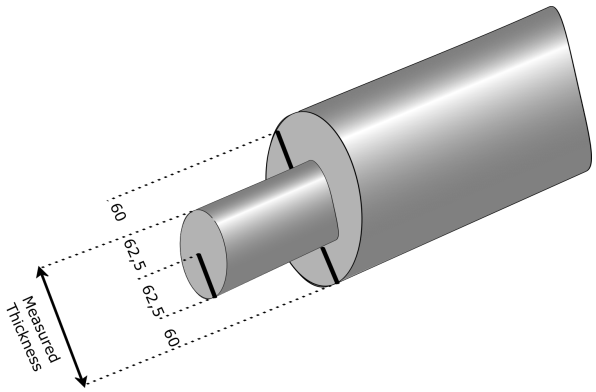

Figure 3.19. Measured thickness of a stripped fiber with 245 μm coating and 125 μm cladding.

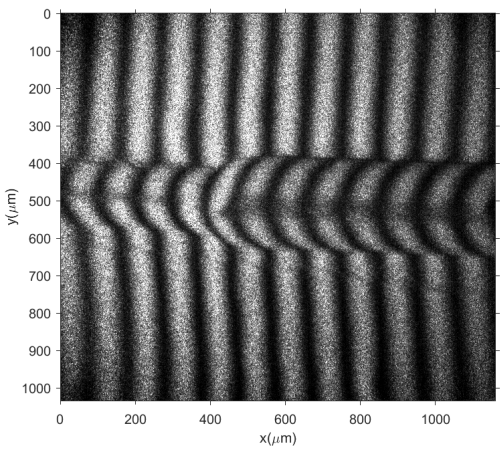

(a) Captured and cropped image.

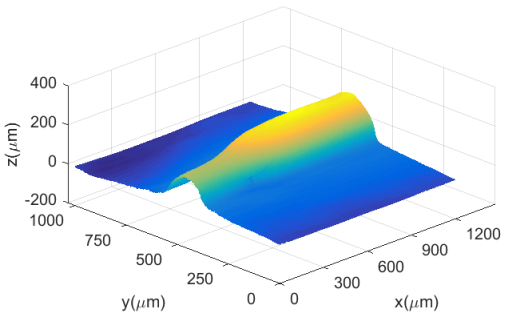

(b) 3D height distribution of the stripped fiber.

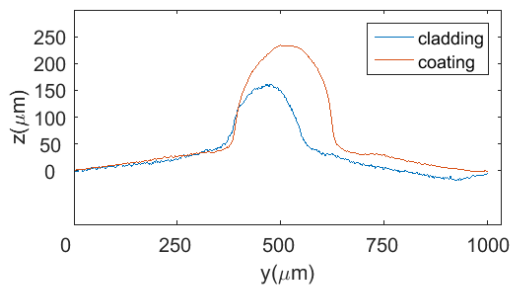

(c) The minima for coating and cladding, 234 ± 7 μm and 162 ± 5 μm respectively.

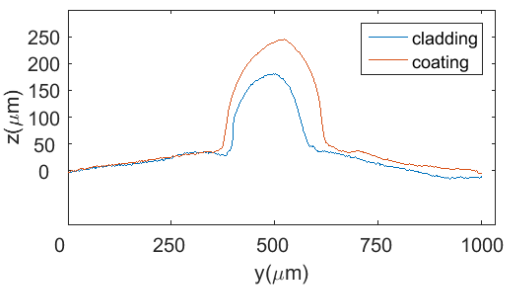

(d) The maxima for coating and cladding, 246 ± 7 μm and 182 ± 5 μm respectively.

Figure 3.20. Height distribution and cross sections of a partially stripped fiber optic cable which has 245 ± 15 μm coating and 125 ± 1 μm cladding.

These result also suffer the errors resulted from the correction fluid thickness since the lack of the correction fluid again is seen on the peaks of both parts of the fiber verifed by the shaded line in Figure 3.20(a). It is seen that the lowering effect caused by the absence of correction fluid on the coating is canceled, raised by the ± 15 μm fluctuation on the thickness of the coating itself. This coincidence gives the results that both minimum, 234 ± 7 μm, and maximum,246 ± 7 μm, measurements are on the order of one sigma away from the expected value 245 μm. However, since the diameter and the uncertainty of the cladding is 125 ± 1 μm, the lowering effect resulted from the lack of correction fluid is evident. The expected value is 185 ± 5 μm as stated before but the minimum and the maximum values are 162 ± 5 μm and 182 ± 5 μm respectively. The maximum value for the stripped part of the fiber is in the coordinate $x = 341$ μm where it is seen that there is no shaded are on the fringe line and the correction fluid is applied correctly whereas 162 ± 5 μ is measured from the shaded part and is around 20 μm away from the expected value. All the fiber specs in this thesis are taken from [75].

Other than experiments with fiber optic cables that require correction fluid or a lacquer for smooth transitions between the reference plane and the edge of them, measurements are also taken for objects like one Turkish lira that does not require any lacquer on it. Studied patterns at the back side of the coin are encircled in red in Figure 3.21.

Figure 3.21. Selected regions on a one Turkish lira to study the height distributions.

Captured and cropped image, the height distribution and profiles of cross sections of the letter C and the disk patterns on the coin are in Figure 3.22 and Figure 3.23 respectively. It is in agreement with the results of the coin measurements here [77].

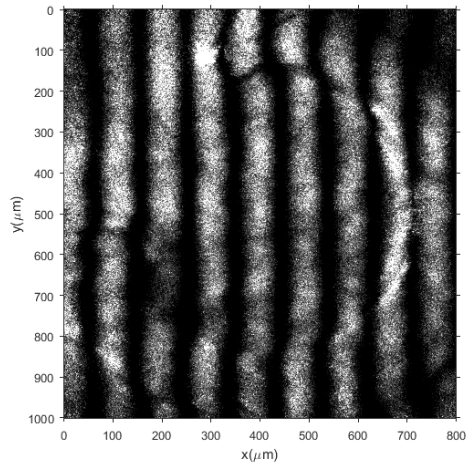

(a) Captured and cropped image.

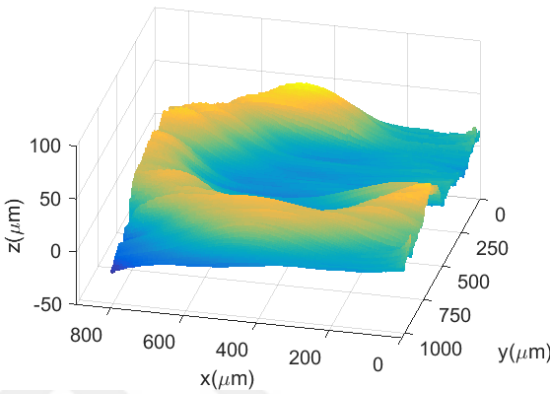

(b) 3D height distribution of the letter C.

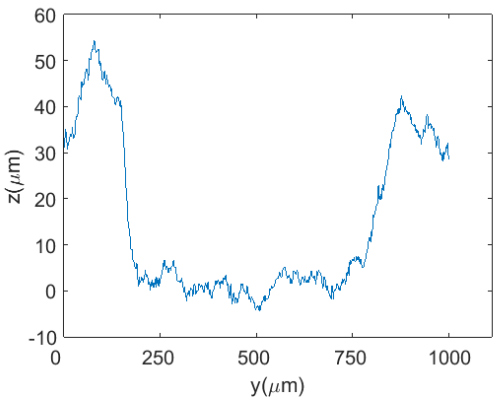

(c) Profile of a cross section at $x = 445\ \mu m$.

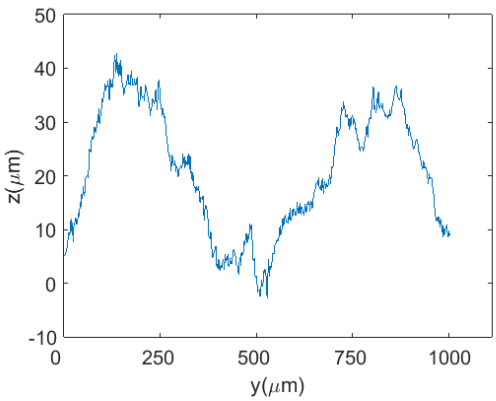

(d) Profile of a cross section at $x = 622\ \mu m$.

Figure 3.22. Height distribution and profiles of cross sections of the letter C on a one Turkish lira.

It is also seen from Figure 3.23(c) that we have a deviation on the order of 5 μm, as measured before, for the flat surface of the disk pattern. Also the captured image and the height distribution of letter H are given in Figure 3.24. We cropped and eliminate some of the discontinuities at the edges of the letters since there is no lacquer used to correct them as in the fiber measurements.

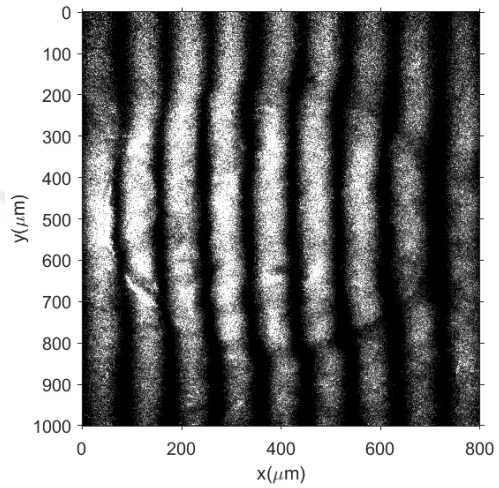

(a) Captured and cropped image.

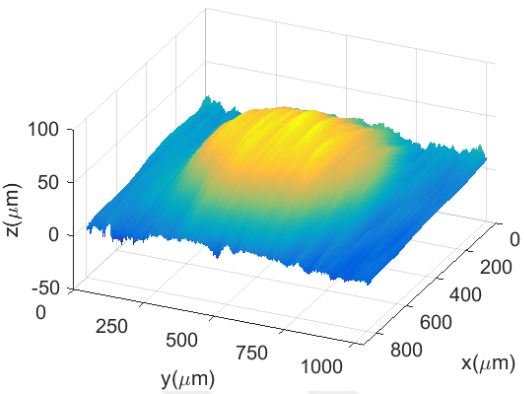

(b) 3D height distribution of the disk pattern.

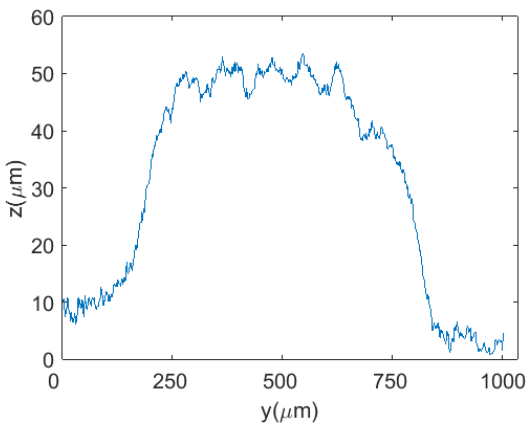

(c) Profile of a cross section at $x = 356\ \mu m$.

Figure 3.23. Height distribution and a crossection profile of the disk pattern on a one Turkish lira.

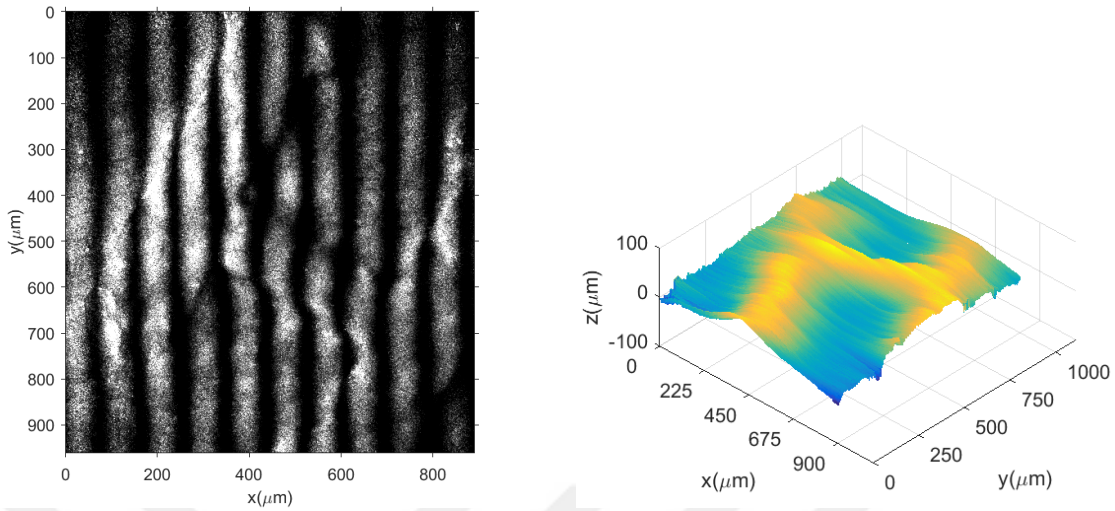

(a) Captured and cropped image.

(b) 3D height distribution of the letter H.

Figure 3.24. Height distribution of the letter H on a one Turkish lira.

Images taken in this thesis are captured with Optronis Cr600x2 CCD camera at 1280x 1024 resolution, and analysed using Matlab 2015a. Figures without citations are either produced by the Matlab or drawn using Inkscape with the help of Clipart and Component library [61].

4. CONCLUSION

It is shown that a simple modification on the Lloyd's mirror assembly achives height distribution extraction at micron scale without using any optical element for the fringe projection except a micrometer stage and a microscope for image acquisition. In this setup, also the fringe frequency is easily controllable using the micrometer stage and adjusting the separation between the mirror and the fiber.

For the analysis, it is concluded that 1D CWT with using morlet wavelet as the mother wavelet is sufficient to use the power of the wavelet transform for different objects with different height distributions. Also it is proven that the reference subtraction is more reliable than the plane fitting method when flat fringes, which are not affected by the test objects, are not present on a region in the captured image of the test object. If it is difficult to use the method of triangulation for phase to height conversion, a simple approach for the conversion and a calibration technique is proven to be suitable for the desired objective.

Our measurements show that we have a standard deviation on the order of 5 μm. However, while the objects are measured with 5 μm precision, the fiber measurements are not very accurate due to the correction fluid thickness. Since we are at micron scale, its thickness affects the accuracy of our measurements. By looking at the errors and the smoothness of the shapes of the objects, it is regarded as accurate if the effect of the correction fluid is eliminated which is on the order of 20 μm. This effect can be eliminated with the use of a standard lacquer that has a good precision at micron scale thickness. The 5 μm error can also be lowered by using a more sensitive stage, for example, using a nanopositioning stage rather than using a microscope stage. Along with these improvements for a future work, a telecentric lens with higher field of view can be used to cover wider areas and to prevent loss of focus in some regions on the field of view.

Additionally, since using the micrometer stage on the microscope has negligible effect on the fringe frequency, it can be used as a tool for phase shifting profilometry like in Mirau interferometer. Then it would be possible to combine the phase maps for both wavelet transform and the phase shifting profilometry for better results.

REFERENCES

1. Cui, H., N. Dai, W. Liao and X. Cheng, "Intraoral 3D optical measurement system for tooth restoration", *Optik-International Journal for Light and Electron Optics*, Vol. 124, No. 12, pp. 1142–1147, 2013.

2. Kumar, R., V. Srivastava, D. S. Mehta and C. Shakher, "Role of Arbitrary Intensity Profile Laser Beam in Trapping of RBC for Phase-imaging", *Journal of the Optical Society of Korea*, Vol. 20, No. 1, pp. 78–87, 2016.

3. Larimer, C., J. D. Suter, G. Bonheyo and R. S. Addleman, "In situ non-destructive measurement of biofilm thickness and topology in an interferometric optical microscope", *Journal of biophotonics*, Vol. 9, No. 6, pp. 656–666, 2016.

4. Zhang, Y., J.-y. Hu, J.-l. Li, H.-q. Wang *et al.*, "The application of WTP in 3-D reconstruction of train wheel surface and tread defect", *Optik-International Journal for Light and Electron Optics*, Vol. 131, pp. 749–753, 2017.

5. Weckenmann, A. and J. Weickmann, "Optical inspection of formed sheet metal parts applying fringe projection systems and virtual fixation", *Metrology and Measurement Systems*, Vol. 13, No. 4, pp. 321–334, 2006.

6. Rövid, A., "Machine vision-based measurement system for vehicle body inspection", *Acta Polytechnica Hungarica*, Vol. 10, No. 5, pp. 145–158, 2013.

7. Bräuer-Burchardt, C., M. Heinze, I. Schmidt, P. Kühmstedt and G. Notni, "Underwater 3D surface measurement using fringe projection based scanning devices", *Sensors*, Vol. 16, No. 1, p. 13, 2015.

8. Takeda, M., H. Ina and S. Kobayashi, "Fourier-transform method of fringe-pattern analysis for computer-based topography and interferometry", *JosA*, Vol. 72, No. 1, pp. 156–160, 1982.

9. Malacara, D., *Optical shop testing*, Vol. 59, John Wiley & Sons, 2007.

10. Azcona Guerrero, F. J., R. Atashkhooei and S. Royo Royo, "Differential optical feedback interferometry for the measurement of nanometric displacements", *Óptica pura y aplicada*, Vol. 47, No. 1, pp. 19–25, 2014.

11. Chung, S., *Measuring Human Chromosomes using Confocal microscopy and Ptychography*, 2015, `http://www.ucl.ac.uk/~ucapikr/projects/Sumin_submit_email.pdf`, accessed at July 2017.

12. Li, D., C. Liu and J. Tian, "Telecentric 3D profilometry based on phase-shifting fringe projection", *Optics express*, Vol. 22, No. 26, pp. 31826–31835, 2014.

13. Islam, N., R. Parkin, M. Jackson and P. Mueller, *A novel surface profile measurement system*, Loughborough University, 2009.

14. Zhong, M., X. Su, W. Chen, Z. You, M. Lu and H. Jing, "Modulation measuring profilometry with auto-synchronous phase shifting and vertical scanning", *Optics express*, Vol. 22, No. 26, pp. 31620–31634, 2014.

15. Yılmaz, Ö. K., E. Coşkun and S. Özder, "Generalized Morse wavelets for the phase evaluation of projected fringe pattern", *Measurement Science and Technology*, Vol. 25, No. 10, p. 105701, 2014.

16. Gorthi, S. S. and P. Rastogi, "Fringe projection techniques: whither we are?", *Optics and lasers in engineering*, Vol. 48, No. IMAC-REVIEW-2009-001, pp. 133–140, 2010.

17. Suzuki, T., R. Kiyohara, M. Ichikawa and O. Sasaki, "Interference fringe analysis using wavelet transform", *Proc. SPIE*, Vol. 7160, pp. 716002–716002–12, 2008.

18. Liebling, M., T.-F. Bernhard, A. H. Bachmann, L. Froehly, T. Lasser and M. Unser, "Continuous wavelet transform ridge extraction for spectral interferometry imag-

ing", *Biomedical Optics 2005*, pp. 397–402, International Society for Optics and Photonics, 2005.

19. Hecht, E., "Optics, 4th", *International edition, Addison-Wesley, San Francisco*, Vol. 3, 2002.

20. Park, C.-S., K.-W. Park, U. Jung, J. Kim, S.-W. Kang and H.-R. Kim, "Dynamic fringe pattern generation using an electrically tunable liquid crystal Fabry-Perot cell for a miniaturized optical 3-D surface scanning profilometer", *Molecular Crystals and Liquid Crystals*, Vol. 526, No. 1, pp. 28–37, 2010.

21. Bulut, K. and M. N. Inci, "Three-dimensional optical profilometry using a four-core optical fibre", *Optics & Laser Technology*, Vol. 37, No. 6, pp. 463–469, 2005.

22. Pennington, T. L., H. Xiao, R. May and A. Wang, "Miniaturized 3-D surface profilometer using a fiber optic coupler", *Optics & Laser Technology*, Vol. 33, No. 5, pp. 313–320, 2001.

23. Windecker, R., M. Fleischer and H. J. Tiziani, "Three-dimensional topometry with stereo microscopes", *Optical Engineering*, Vol. 36, No. 12, pp. 3372–3377, 1997.

24. Choi, Y.-B. and S.-W. Kim, "Phase-shifting grating projection moiré topography", *Optical Engineering*, Vol. 37, No. 3, pp. 1005–1010, 1998.

25. Zhou, D., Z. Wang, N. Gao, Z. Zhang and X. Jiang, "Virtual fringe projection system with nonparallel illumination based on iteration", *Measurement Science and Technology*, Vol. 28, No. 6, p. 065201, 2017.

26. Vairavan, R., V. Retnasamy, M. M. Shahimin, Z. Sauli, L. S. Leng, W. M. W. Norhaimi, R. Marimuthu, O. Abdullah and S. Kirtsaeng, "3D Mapping of Breast Surface Using Digital Fringe Projection", *Proc. of SPIE Vol*, Vol. 10043, pp. 1004315–1, 2017.

27. Li, B. and S. Zhang, "Microscopic structured light 3d profilometry: Binary defocusing technique vs. sinusoidal fringe projection", *Optics and Lasers in Engineering*, Vol. 96, pp. 117–123, 2017.

28. Chen, L., C. Cho and X. Nguyen, "One-shot three-dimensional surface profilometry using DMD-based two-frequency moiré and Fourier transform technique", *International Journal on Smart Sensing and Intelligent Systems*, Vol. 2, No. 3, pp. 345–380, 2009.

29. Cheng, N.-J., S.-Y. Chen and W.-H. Su, "Phase unwrapping using binary-encoded fringe pattern for phase-shifting projected fringe profilometry", *SPIE Optical Engineering+ Applications*, pp. 995819–995819, International Society for Optics and Photonics, 2016.

30. Lei, S. and S. Zhang, "Flexible 3-D shape measurement using projector defocusing", *Optics letters*, Vol. 34, No. 20, pp. 3080–3082, 2009.

31. Ayubi, G. A., J. M. Di Martino, J. R. Alonso, A. Fernández, C. D. Perciante and J. A. Ferrari, "Three-dimensional profiling with binary fringes using phase-shifting interferometry algorithms", *Applied Optics*, Vol. 50, No. 2, pp. 147–154, 2011.

32. Budianto, B. and D. P. Lun, "Efficient 3-dimensional model reconstruction based on marker encoded fringe projection profilometry", *Acoustics, Speech and Signal Processing (ICASSP), 2014 IEEE International Conference on*, pp. 574–578, IEEE, 2014.

33. Pan, J., P. S. Huang and F.-P. Chiang, "Color-coded binary fringe projection technique for 3-D shape measurement", *Optical Engineering*, Vol. 44, No. 2, pp. 023606–023606, 2005.

34. Salvi, J., S. Fernandez, T. Pribanic and X. Llado, "A state of the art in structured light patterns for surface profilometry", *Pattern recognition*, Vol. 43, No. 8, pp. 2666–2680, 2010.

35. Kart, T., G. Kösoğlu, H. Yüksel and M. N. İnci, "Fourier transform optical profilometry using fiber optic Lloyd's mirrors", *Applied optics*, Vol. 53, No. 35, pp. 8175–8181, 2014.

36. Gåsvik, K. J., *Optical metrology*, John Wiley & Sons, 2003.

37. YILMAZ, Ö. K., "Determination of height profile from a two-dimensional fringe signal using a two-dimensional continuous wavelet transform", *Turkish Journal of Physics*, Vol. 41, No. 1, pp. 81–89, 2017.

38. Novák, J., "Methods for 2-D phase unwrapping in MATLAB", *Proc. MATLAB 2001*, pp. 313–317, VSCHT Publishing, 2001.

39. Lu, J., R. Mo, H. Sun and Z. Chang, "Flexible calibration of phase-to-height conversion in fringe projection profilometry", *Applied Optics*, Vol. 55, No. 23, pp. 6381–6388, 2016.

40. Kemao, Q., "Windowed Fourier transform for fringe pattern analysis", *Applied Optics*, Vol. 43, No. 13, pp. 2695–2702, 2004.

41. Vanlanduit, S., J. Vanherzeele, P. Guillaume, B. Cauberghe and P. Verboven, "Fourier fringe processing by use of an interpolated Fourier-transform technique", *Applied optics*, Vol. 43, No. 27, pp. 5206–5213, 2004.

42. Vanherzeele, J., S. Vanlanduit and P. Guillaume, "Processing optical measurements using a regressive Fourier series: A review", *Optics and Lasers in Engineering*, Vol. 47, No. 3, pp. 461–472, 2009.

43. Hyok Jong, K. and C. S. Kim, "Determination of the local contrast of interference fringe patterns using continuous wavelet transform", *ArXiv e-prints*, 2014.

44. Gorthi, S. S. and K. R. Lolla, "Wavelet transform analysis of truncated fringe patterns in 3-D surface profilometry", *Optical Metrology*, pp. 265–273, International

Society for Optics and Photonics, 2005.

45. Torrence, C. and G. P. Compo, "A practical guide to wavelet analysis", *Bulletin of the American Meteorological society*, Vol. 79, No. 1, pp. 61–78, 1998.

46. Dursun, A., S. Özder and F. N. Ecevit, "Continuous wavelet transform analysis of projected fringe patterns", *Measurement Science and Technology*, Vol. 15, No. 9, p. 1768, 2004.

47. Addison, P. S., "Wavelet transforms and the ECG: a review", *Physiological measurement*, Vol. 26, No. 5, p. R155, 2005.

48. Meyers, S. D., B. G. Kelly and J. J. O'Brien, "An introduction to wavelet analysis in oceanography and meteorology: With application to the dispersion of Yanai waves", *Monthly weather review*, Vol. 121, No. 10, pp. 2858–2866, 1993.

49. Chew, W. C., *Waves and fields in inhomogeneous media*, Vol. 522, IEEE press New York, 1995.

50. Zhang, Z. and J. Zhong, "Applicability analysis of wavelet-transform profilometry", *Optics express*, Vol. 21, No. 16, pp. 18777–18796, 2013.

51. Gdeisat, M. A., A. Abid, D. R. Burton, M. J. Lalor, F. Lilley, C. Moore and M. Qudeisat, "Spatial and temporal carrier fringe pattern demodulation using the one-dimensional continuous wavelet transform: recent progress, challenges, and suggested developments", *Optics and Lasers in Engineering*, Vol. 47, No. 12, pp. 1348–1361, 2009.

52. Quan, C., C. Tay and L. Chen, "A study on carrier-removal techniques in fringe projection profilometry", *Optics & Laser Technology*, Vol. 39, No. 6, pp. 1155–1161, 2007.

53. Yue, H., Y. Wu, B. Zhao, Z. Ou, Y. Liu and Y. Liu, "A carrier removal method in

phase measuring deflectometry based on the analytical carrier phase description", *Optics express*, Vol. 21, No. 19, pp. 21756–21765, 2013.

54. Chen, L. and C. J. Tay, "Carrier phase component removal: a generalized least-squares approach", *JOSA A*, Vol. 23, No. 2, pp. 435–443, 2006.

55. Miao, H., C. Quan, C. J. Tay and Y. Fu, "Analysis of phase distortion in phase-shifted fringe projection", *Optics and lasers in engineering*, Vol. 45, No. 2, pp. 318–325, 2007.

56. Afifi, M., A. Fassi-Fihri, M. Marjane, K. Nassim, M. Sidki and S. Rachafi, "Paul wavelet-based algorithm for optical phase distribution evaluation", *Optics communications*, Vol. 211, No. 1, pp. 47–51, 2002.

57. Bailich, M., M. Bahich and M. Benaissa Bellach, "Numerical Investigation of Phase Estimation for 3D Measurement in the Fringe Projection Technology", *Citeseer*, 2013.

58. Olhede, S. C. and A. T. Walden, "Generalized morse wavelets", *IEEE Transactions on Signal Processing*, Vol. 50, No. 11, pp. 2661–2670, 2002.

59. Kösoğlu, G., H. Yüksel and M. N. Inci, "Phase stepping optical profilometry using fiber optic Lloyd's mirrors", *Applied optics*, Vol. 55, No. 4, pp. 846–852, 2016.

60. Corporation, N., *Layout 1*, 2012, `http://assets.newport.com/webdocuments-en/images/app_note_49_lloyds_mirror_interf.pdf`, accessed at July 2017.

61. Franzen, A., *ComponentLibrary: a free vector graphics library for optics*, 2009, `http://www.gwoptics.org/ComponentLibrary/`, accessed at July 2017.

62. Farge, M., "Wavelet transforms and their applications to turbulence", *Annual review of fluid mechanics*, Vol. 24, No. 1, pp. 395–458, 1992.

63. Pedraza-Ortega, J. C., E. Efren Gorrostieta-Hurtado, M. Delgado-Rosas, S. L. Canchola-Magdaleno, J. M. Ramos-Arreguin, M. A. Aceves Fernandez and A. Sotomayor-Olmedo, "A 3D Sensor Based on a Profilometrical Approach", *Sensors*, Vol. 9, No. 12, pp. 10326–10340, 2009.

64. Zeger, K., "Gaussian.dvi", `http://code.ucsd.edu/zeger/45/Gaussian.pdf`, accessed at July 2017.

65. Jacques, L., A. Coron, P. Vandergheynst and A. Rivoldini, "The YAWTb toolbox : Yet Another Wavelet Toolbox", `http://sites.uclouvain.be/ispgroup/yawtb`, accessed at June 2017.

66. Costantini, M., "A novel phase unwrapping method based on network programming", *IEEE Transactions on geoscience and remote sensing*, Vol. 36, No. 3, pp. 813–821, 1998.

67. Ghiglia, D. C. and L. A. Romero, "Robust two-dimensional weighted and unweighted phase unwrapping that uses fast transforms and iterative methods", *JOSA A*, Vol. 11, No. 1, pp. 107–117, 1994.

68. Luong, B., *Costantini phase unwrapping - File Exchange - MATLAB Central*, August 2009, `https://www.mathworks.com/matlabcentral/fileexchange/25154-costantini-phase-unwrapping?requestedDomain=www.mathworks.com`, accessed at July 2017.

69. Kasim, M. F., "2D Weighted Phase Unwrapping - File Exchange - MATLAB Central", `https://www.mathworks.com/matlabcentral/fileexchange/60345-2d-weighted-phase-unwrapping?focused=7094234&tab=function`, 2016, accessed at July 2017.

70. Liu, Y., *Accuracy improvement of 3D measurement using digital fringe projection*, Master's Thesis, School of Electrical, Computer and Telecommunications Engineering, University of Wollongong, 2011.

71. Rodriguez-Vera, R., K. Genovese, J. Rayas and F. Mendoza-Santoyo, "Calibration of a micro-topographic measurement system based on Talbot fringe projection", *Proc. 2007 SEM Annual Conf. and Exposition on Experimental and Applied Mechanics, paper*, Vol. 83, 2007.

72. Wang, Y., S. Zhang and J. H. Oliver, "3D shape measurement technique for multiple rapidly moving objects", *Optics express*, Vol. 19, No. 9, pp. 8539–8545, 2011.

73. Zhu, F., D. Lei and X. He, "Measurement system of dynamic microscopic deformation for membrane based on fringe projection", *Optical Engineering*, Vol. 52, No. 3, pp. 033604–033604, 2013.

74. An, Y. and S. Zhang, "Three-dimensional absolute shape measurement by combining binary statistical pattern matching with phase-shifting methods", *Applied Optics*, Vol. 56, No. 19, pp. 5418–5426, 2017.

75. Thorlabs, *Single Mode Fiber*, `https://www.thorlabs.com/newgrouppage9.cfm?objectgroup_id=949`, accessed at June 2017.

76. Lyons, B., *PREDICT THE THICKNESS OF PAINT - Carbit Paint Company Blog Archive*, November 2004, `https://carbit.com/predict-thickness-paint`, accessed at July 2017.

77. Yin, Y., M. Wang, B. Z. Gao, X. Liu and X. Peng, "Fringe projection 3D microscopy with the general imaging model", *Optics express*, Vol. 23, No. 5, pp. 6846–6857, 2015.

APPENDIX A: SETUP

The experimental setup in Figure 3.3 is shown in detail on the following page.

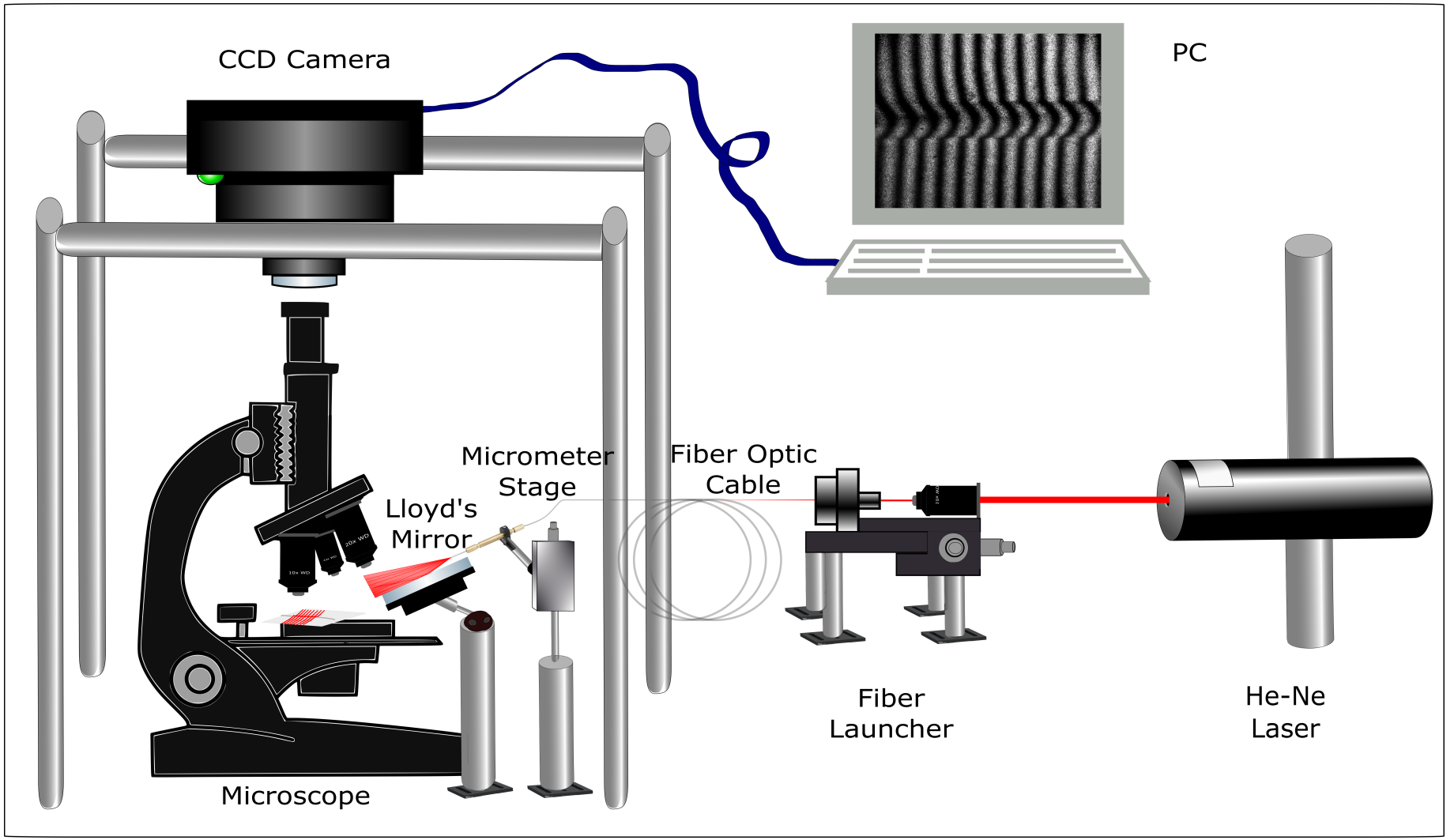

Figure A.1. Our experimental setup in detail.